drones

MDPI

Article

Design and Validation of a 3D-Printed Drone Chassis Model Through Static and Transient Nonlinear FEM Analyses and Experimental Testing

Basil Mohammed Al-Hadithi [1,2,*] and Sergio Alcón Flores [3]

[1] Intelligent Control Group, Universidad Politécnica de Madrid, Centre for Automation and Robotics UPM-CSIC, C/J. Gutierrez Abascal, 2., 28006 Madrid, Spain
[2] Department of Electrical, Electronics, Control Engineering, School of Industrial Design and Engineering, Universidad Politécnica de Madrid, C/Ronda de Valencia, 3., 28012 Madrid, Spain
[3] Department of Mechanical Engineering, School of Industrial Design and Engineering, Universidad Politécnica de Madrid, C/Ronda de Valencia, 3., 28012 Madrid, Spain; s.alcon@alumnos.upm.es
* Correspondence: basil.alhadithi@upm.es

Highlights

What are the main findings?

- A screwless FPV drone chassis with interlocking, interchangeable arms inspired by Japanese joinery was designed in Autodesk Inventor, analyzed through a hierarchical simulation philosophy combining global static analyses validated by simplified linear models, and nonlinear transient simulations for crash and maximum acceleration scenarios using Inventor Nastran.
- The structure was 3D printed in PETG as a rapid prototype to validate the design and analysis methodology, with planned production in carbon fiber to achieve final performance and durability goals.

What are the implications of the main findings?

- The proposed design and validation workflow offer a comprehensive pathway for developing lightweight, crash-resilient sub-250 g UAVs.
- This approach bridges theoretical FEM modeling with real-world performance, enhancing the structural and functional reliability of micro aerial vehicles.

Abstract

This work presents the structural analysis and validation of a sub-250 g FPV drone chassis, emphasizing both theoretical rigor and practical applicability. The novelty of this contribution lies in four complementary aspects. First, the structural philosophy introduces a screwless frame with interchangeable arms, joined through interlocking mechanisms inspired by traditional Japanese joinery. This approach mitigates stress concentrations, reduces weight by eliminating fasteners, and enables rapid arm replacement in the field. Second, validation relies on nonlinear static and transient FEM simulations, explicitly including crash scenarios at 5 m/s, systematically cross-checked with bench tests and instrumented flight trials. Third, unlike most structural studies, the framework integrates firmware (Betaflight), GPS, telemetry, and real flight performance, linking structural reliability with operational robustness. Finally, a practical materials pathway was implemented through a dual-track strategy: PETG for rapid, low-cost prototyping, and carbon fiber composites as the benchmark for production-level performance. Nonlinear transient FEM analyses were carried out using Inventor Nastran under multiple load cases, including maximum motor acceleration, pitch maneuvers, and lateral impact at 40 km/h, and were validated against simplified analytical models. Experimental validation included bench

Academic Editor: Yushu Yu

Received: 27 August 2025
Revised: 26 October 2025
Accepted: 5 November 2025
Published: 12 November 2025

Citation: Al-Hadithi, B.M.; Alcón Flores, S. Design and Validation of a 3D-Printed Drone Chassis Model Through Static and Transient Nonlinear FEM Analyses and Experimental Testing. *Drones* **2025**, *9*, 789. https://doi.org/10.3390/drones9110789

and in-flight trials with integrated telemetry and autonomous features such as Return-to-Home, demonstrating functional robustness. The results show that the prototype flies correctly and that the chassis withstands the loads experienced during flight, including accelerations up to 4.2 G (41.19 m/s^2), abrupt changes in direction, and high-speed maneuvers reaching approximately 116 km/h. Quantitatively, safety factors of approximately 5.3 under maximum thrust and 1.35 during impact confirm sufficient structural integrity for operational conditions. In comparison with prior works reviewed in this study, the key contribution of this work lies in unifying advanced, crash-resilient FEM simulations with firmware-linked flight validation and a scalable material strategy, establishing a distinctive and comprehensive workflow for the development of sub-250 g UAVs.

Keywords: FPV drone; structural analysis; sub-250 g UAV; Finite Element Method (FEM); 3D CAD design; 3D printing; nonlinear simulation; Inventor Nastran; Betaflight firmware; autonomous flight; crash simulation; thrust simulation; hoover simulation; autonomous navigation; GPS Rescue; Return-to-Home

1. Introduction

In recent years, the rapid advancement of unmanned aerial vehicles (UAVs) has led to a surge in the development of compact and efficient drone platforms, particularly in the FPV (First-Person View) community. Among these, sub-250 g drones have gained special attention due to their regulatory advantages, reduced risk profiles, and portability [1]. Many civil aviation authorities, including the FAA and EASA, classify drones under 250 g as exempt from certain registration and operational restrictions, which further motivates both hobbyists and researchers to explore this category of UAVs [2]. However, minimizing weight while maintaining structural integrity and functionality presents significant design challenges, particularly in the context of dynamic flight manoeuvres and potential collisions.

Structural reliability is a critical factor in drone performance, especially for applications involving high-speed FPV racing or autonomous navigation in complex environments. Lightweight UAVs are especially vulnerable to high-frequency vibrations, fatigue-induced cracking, and impact damage, all of which may compromise flight safety and efficiency [3]. Traditional design approaches often rely on empirical testing or oversimplified models, which may not fully capture the nonlinear and transient mechanical behavior of lightweight drone frames. Therefore, integrating modern simulation tools such as Finite Element Method (FEM) analysis into the design workflow becomes essential for predicting structural performance under realistic operating conditions [4]. In this context, digital twin frameworks and multi-physics simulations have been increasingly adopted to shorten development cycles and enhance structural reliability in UAV applications [5].

This article aims to bridge the gap between theoretical structural analysis and practical drone design by conducting a comprehensive evaluation of a sub-250 g FPV drone frame. Nonlinear static and transient simulations were carried out using Autodesk Inventor Nastran 2025, and the results were compared with simplified analytical models to verify their accuracy and reliability. In addition, the physical prototype was fabricated using 3D printing technologies and integrated with Betaflight firmware 4.5.1, enabling autonomous features such as Return-to-Home (RTH) [6]. Beyond validation, such a workflow demonstrates the potential of simulation-driven design for rapid iteration in UAV development [7].

To facilitate rapid prototyping and accessible fabrication, the frame was initially designed for 3D printing using PETG filament. PETG offers a good balance between mechanical strength, flexibility, and ease of use with consumer-grade FDM printers, making it suitable for iterative development in a home or laboratory setting. Its moderate impact resistance and durability allowed for functional testing of the structural concept without specialized manufacturing equipment. However, for high-performance or production versions, carbon fiber composites represent a more appropriate material choice. PETG-based designs—even when reinforced with short carbon fibers—offer improved mechanical properties (e.g., approximately 23% increase in yield strength over neat PETG) but remain substantially inferior in specific stiffness and vibration resistance compared to pure carbon fiber frames [1]. A carbon fiber composite structure delivers significantly higher Young's modulus and strength-to-weight ratio, which are critical for improving flight dynamics, energy efficiency, and crash resilience in FPV drones, despite its greater fabrication complexity and cost [8].

The main objective of this work is to develop and validate a structurally optimized, lightweight FPV drone frame capable of withstanding demanding mechanical stresses during flight. The outcomes contribute not only to the design methodology of small UAVs but also to the understanding of lightweight structural behavior in dynamic applications. Furthermore, this research highlights how combining additive manufacturing with advanced composite materials can expand the design space for sub-250 g UAVs in both hobbyist and professional domains [9]. A video demonstration of the prototype in autonomous flight is provided to illustrate the effectiveness of the proposed design approach.

To provide a clear roadmap for the reader, the specific research objectives of this study are summarized as follows:

- To analyze and model the structural behavior of a sub-250 g FPV drone frame using both analytical methods and Finite Element Methods.
- To evaluate the performance of additively manufactured (PETG-based) and composite (carbon fiber) frames under realistic flight and impact conditions.
- To validate simulation results through experimental testing and prototype flight performance.
- To propose a simulation-driven workflow that integrates FEM and digital twin concepts for lightweight UAV design optimization.
- Regulatory motivation: Operating below the 250 g threshold has significant implications under both EASA and FAA frameworks. Under the EASA Open Category, as defined in Commission Implementing Regulation (EU) 2019/947 and Delegated Regulation (EU) 2019/945, UAS with a Maximum Take-Off Mass (MTOM) of <250 g (Class C0) may be flown in subcategory A1 with minimal training requirements and, in many cases, without operator registration. Similarly, under FAA regulations (14 CFR Part 48), drones weighing less than 0.55 lb (≈250 g) used for recreational purposes are not required to be registered. Designing for the sub-250 g segment therefore enables broader and less encumbered deployment; however, the reduced mass budget imposes strict structural efficiency demands, justifying advanced simulation, material selection, and integrated performance validation.

Finally, the organization of this paper is as follows: Section 2 details the methodological framework, including prior work positioning, design tools, simulation environment, and validation protocols. Section 3 presents the outcomes of the chassis design, modeling, and fabrication, together with the structural analyses conducted through the Finite Element Method (FEM) under different flight conditions. Section 4 discusses the main limitations of the study, addressing modeling assumptions, experimental scope, and material constraints that may influence the generalization of results. Section 5 summarizes the main findings of

this work, highlighting the validated structural performance of the proposed sub-250 g FPV drone, and outlines future research directions aimed at improving materials, integration, and autonomous flight capabilities.

2. Materials and Methods

This section details the methodological framework adopted to design, simulate, and validate the proposed FPV sub-250 g UAV frame. The approach combines a review of prior work with comparative positioning, followed by the specification of the design tools, material assumptions, simulation environment, fabrication workflow, and validation protocols. Through this structure, the methodology ensures both theoretical consistency and practical relevance, bridging numerical models with experimental testing and real-flight performance.

2.1. Positioning and Contributions Relative to Prior Work

The work presented in [10] published in (MDPI, 2022), is an important reference within UAV chassis design and validation. Its main contribution lies in demonstrating, through linear static analysis and comparison of 3D-printable materials (PLA, ABS, ASA), the feasibility of modular lightweight structures in general UAV contexts [10]. This conceptual approach has provided a methodological baseline for subsequent developments, underlining the importance of considering both structural design and material properties from the early stages [11].

Much of the academic literature on UAV frames has followed a similar path, focusing on static or modal FEM, topology optimization, or comparative studies of polymers and composites [12]. Contributions as [13] have been essential to establish a reference framework, yet in many cases they remain primarily theoretical, with limited experimental validation or integration into actual flight systems [14].

2.1.1. Specific Orientation of This Research

This work builds on this foundation while advancing a differentiated approach, tailored to the sub-250 g FPV segment, where regulatory constraints and performance demands are uniquely stringent. It contributes several defining aspects:

1. **Structural philosophy:** A frame with interchangeable arms assembled without screws, using joinery-inspired interlocks reminiscent of Japanese marquetry. This design mitigates stress concentrations, reduces weight by eliminating fasteners, and enables rapid arm replacement in the field.
2. **Methodology of validation:** Nonlinear static and transient FEM simulations, including crash scenarios at $\sim$5 m/s, validated against physical bench tests and instrumented flight trials.
3. **Integration of system operation:** Unlike most structural studies, our design and validation explicitly consider firmware (Betaflight), GPS, telemetry, and real-flight performance.
4. **Practical materials pathway:** Accessible PETG for rapid prototyping and iteration, combined with CFRP for the production-ready high-performance frame.
5. **Regulatory motivation:** Operating below the 250 g threshold has significant implications under both EASA and FAA frameworks [15]. Under the EASA Open Category, as defined in Commission Implementing Regulation (EU) 2019/947 and Delegated Regulation (EU) 2019/945, UAS with a Maximum Take-Off Mass (MTOM) of <250 g (Class C0) may be flown in subcategory A1 with minimal training requirements and, in many cases, without operator registration. Similarly, under FAA regulations (14 CFR Part 48), drones weighing less than 0.55 lb ($\approx$250 g) used for recreational pur-

poses are not required to be registered. Designing for the sub-250 g segment therefore enables broader and less encumbered deployment; however, the reduced mass budget imposes strict structural efficiency demands, justifying advanced simulation, material selection, and integrated performance validation [16].

2.1.2. Comparison of the Proposed Method with Other Works

The work given in [10] provides a valuable baseline that integrates *linear static FEA* and *additive manufacturing* within a coherent workflow. Our work complements that contribution by extending the analysis to *nonlinear dynamics and crash transients* with experimental and in-flight validation. In [12], an elegant *unibody* approach is proposed via topology optimization and DFAM to reduce assembly weight and complexity. In contrast, though complementary, our chassis emphasizes *interchangeability and maintainability* with screwless joints. Widely cited studies such as [11,13] provide essential baselines through FEM of conventional or 3D-printed frames, which are generally static and simulation-driven; our work expands this by adding *transient, impact-oriented FEM* tied to flight data. The CogniFly platform illustrates collision-resilient design with semi-rigid joints, while the suggested work differs by channeling impact energy through joinery-inspired arm interfaces to diffuse stresses and enable quick replacement [17]. Finally, recent integrated workflows of topology optimization and AM highlight the importance of computational geometry, while our contribution adds the *practical axis of repairability and dynamic validation* [14].

When compared along four main axes—*frame philosophy*, *analysis scope*, *validation/evidence*, and *materials and manufacturing*—these distinctions become clearer. From the perspective of frame philosophy, our proposed work (FPV sub-250 g) adopts a repair-first design with interchangeable arms and screwless joints inspired by Japanese joinery. A modular CAD-based philosophy is presented with 3D-printed prototypes in [10], while a unibody/monocoque layout exploiting DFAM is developed in [12]. In [11], plate-and-arm assemblies are applied. A 3D-printed configuration is explored in [13]. A collision resilience is emphasized in [17], and the authors of [14] opted for optimization-driven geometries.

In terms of analysis scope, our work extends beyond static checks into *nonlinear transient FEM* that couples structural analysis with firmware and FPV flight constraints. The work developed in [10] is restricted to linear static FEA, while the one given in [12] focused on topology optimization. Static and modal/explicit FEM is included in [11]. The authors in [13] confined themselves to CAD and static FEM feasibility. In [17], empirical crash design is prioritized and an integrated topology optimization without FPV dynamics is used in [14].

For validation, our approach uniquely integrates bench-loading and in-flight telemetry, directly correlating FEM predictions with flight performance. In [10], CAD/FEA trade-offs and fabrication demos are presented; meanwhile, in [12], they are validated through AM demos and structural targets. The works [11,13] presented mainly simulation-driven results. Resilience up to 7 m/s crashes is verified in [17], while a validated methodology without dynamic flight tests is presented in [14].

Finally, regarding materials and manufacturing, our dual-track strategy employs PETG for rapid, low-cost prototyping and CFRP as a production benchmark. Thermoplastic AM is emphasized in [10,13]. The work in [12] focused on DFAM-driven AM structures, while in [11] conventional materials are considered. Leveraged low-cost resilient plastics are used in [17] and optimization methodologies anchored in AM are developed in [14].

Taken together, these comparative insights are synthesized visually in Table 1, which condenses the landscape into a structured format.

Summary of contributions.

1. Screwless, interchangeable-arm frame inspired by Japanese joinery.

2. Nonlinear transient FEM for FPV-realistic maneuvers and crash impacts.
3. Dual-track materials strategy: PETG for low-cost prototyping, with CFRP as production benchmark.
4. Bench and in-flight validation with telemetry, GPSm and firmware integration.

Table 1. Comparison of the proposed method with other works.

Work	Frame Philosophy	Analysis Scope	Validation/Evidence	Materials/Mfg. Focus
Proposed work (FPV sub-250 g)	Interchangeable arms; screwless, Japanese-joinery-inspired interfaces; repair-first design	Nonlinear transient FEM; static checks; firmware/flight constraints	Bench loading vs. FEM; in-flight telemetry validation	PETG for prototyping; CFRP for production
MohamedZain et al. (2022) [10]	Modular via generative CAD; 3D-printed prototypes	Linear static FEA	CAD/FEA trade-off; fabrication demo	Thermoplastic AM
Nvss et al. (2022) [12]	Unibody/monocoque; DFAM for reduced assembly	Topology optimization	AM demo; structural targets	Additive manufacturing focus
Singh et al. (2020) [11]	Conventional plate-and-arm	FEM (static; modal/explicit parts)	Simulation-driven, limited experiments	Generic manufacturing
Shelare et al. (2021) [13]	3D-printed drone	CAD and static FEM	Numerical with print feasibility	Thermoplastic AM
CogniFly (Azambuja et al., 2021) [17]	Collision-resilient, semi-rigid	Empirical design, crash focus	Survives $\leq$7 m/s collisions	Low-cost materials
Al-Haddad et al. (2024) [14]	Optimization-driven frame layout	Topology optimization and AM	Method validation (no FPV flight dynamics)	AM methodology

2.2. Design and Simulation Environment

The FPV drone frame was designed using Autodesk Inventor Professional 2025. The model was parametrically constructed to optimize weight and structural integrity while complying with the sub-250 g regulatory requirement. Finite Element Method (FEM) analysis was conducted in Autodesk Inventor Nastran 2025, enabling nonlinear static and transient simulations. The Von Mises yield criterion was applied to assess failure risk under various loading scenarios, including dynamic impacts and sustained thrust loads.

2.3. Material Properties and Assumptions

Frames were fabricated via FDM (Fused Deposition Modeling) using PETG filament. The mechanical properties of PETG are anisotropic due to layer-dependent behavior. Specifically, properties along the XY plane (parallel to print layers) are superior to those along the Z axis (perpendicular to layers) because of reduced interlayer bonding. For conservative and simplified analysis, isotropic behavior was assumed using the minimum values from the XY plane.

In reality, FDM-printed PETG exhibits marked anisotropy, as tensile and shear strengths in the Z-direction may be up to 40–60% lower than those in the XY plane due to weaker interlayer adhesion [18]. The bonding quality depends on extrusion temperature, print speed, and layer height, leading to orthotropic mechanical behavior. A more accurate representation would therefore employ an orthotropic or transversely isotropic model, capturing the directional dependence of stiffness and failure modes such as layer delamination or shear failure between deposited layers. However, the isotropic simplification adopted here provides a conservative lower-bound estimate of frame stiffness and strength, suitable for preliminary structural validation and ensuring safety under all flight conditions.

Table 2 presents a comparison between PETG and the typical values of carbon fiber composites commonly used in FPV drone frames. The CFRP material considered corresponds to a quasi-isotropic laminate composed of unidirectional (UD) carbon fiber/epoxy prepreg layers arranged in a [0/90/±45]s layup [19]. This configuration provides balanced in-plane stiffness, which is representative of typical FPV frame plates manufactured by CNC milling from cured composite sheets [20].

Table 2. Mechanical properties of PETG (FDM-printed) vs. carbon fiber composite (CFRP, quasi-isotropic layup [0/90/±45]s).

Property	PETG (XY Plane)	CFRP (Quasi-Isotropic [0/90/±45]s)	Units
Young's Modulus (E)	2100	135,000	MPa
Tensile Strength	50	600	MPa
Yield Strength (0.2% offset)	40	320	MPa
Elongation at Break	15	1.8	%
Density	1270	1550	kg/m^3
Poisson's Ratio	0.38	0.33	–
Shear Modulus	760	54,000	MPa
Plastic Behavior	Elastic—perfectly plastic	Linear elastic	–

The relatively low modulus and strength of PETG compared to carbon fiber result in lower stiffness and impact resistance, which must be considered in high-performance applications. Nevertheless, PETG provides advantages in ease of fabrication, prototyping flexibility, and cost, making it suitable for iterative development. All structural components were 3D-printed with their main load-bearing axes aligned parallel to the XY plane of the printer bed, ensuring that the filament deposition direction coincides with the principal stress paths and thus maximizes in-plane strength and stiffness. Failure analysis employed the Von Mises criterion using the minimum mechanical values to ensure conservative structural predictions.

Although the analyses were carried out using PETG, the final production configuration is intended to be manufactured in carbon fiber composite. The use of PETG provides a conservative lower-bound validation of the mechanical behavior while simplifying computation and experimental testing. Since carbon fiber exhibits significantly higher stiffness and strength (as shown in Table 2), any design that meets safety requirements in PETG will present even lower deformation and higher safety margins when produced in carbon fiber. To support this assumption, an additional static simulation using the quasi-isotropic CFRP layup has been included, confirming the expected reduction in displacement and increase in the safety factor.

2.4. Simulation Parameters and Load Cases

Finite element meshes used tetrahedral elements with local refinement in stress concentration zones. Static simulations modeled thrust and motor-induced torsion, while transient dynamic analyses simulated impact events at 5 m/s against rigid boundaries. Convergence analysis ensured mesh independence. Loads were calculated based on the expected thrust-to-weight ratios of FPV drones under typical flight conditions.

2.5. Fabrication and Assembly

The frame was printed using an Artillery Genius FDM printer with 100% infill, 0.2 mm layer height, and a 0.4 mm nozzle. Slicing and print preparation were conducted using Ultimaker Cura 5.8. Post-print finishing was minimal to preserve dimensional fidelity. The assembled drone included the following:

- Flight Controller (FC): SpeedyBee F405 AIO
- Firmware: Betaflight 4.5.2
- GPS Module: M10 series
- Digital Video Transmitter (VTX): DJI-compatible system
- Audible Beeper for fail-safe events

Firmware configuration included enabling autonomous Return-to-Home (RTH) and fail-safe protocols using Betaflight Configurator. PID tuning was adjusted for low-mass dynamics and frame-specific resonance.

2.6. Experimental Validation

Static tests involved controlled loading of the frame using known weights at key points to validate FEM predictions. Flight testing evaluated frame response under typical FPV manoeuvres, including high-speed turns, ascents, and controlled impacts. GPS telemetry and flight logs were recorded for analysis.

2.7. Ethical and Data Availability Statements

No human or animal testing was involved. All CAD models, simulation files, and firmware configurations are available upon request and will be published in an open-access repository prior to publication. No restrictions apply to the sharing of materials or data.

3. Results

The design of a customized chassis for unmanned aerial systems (UAS) demands the seamless integration of mechanical, functional, and electronic requirements. This chapter presents a comprehensive account of the *design, modeling, manufacturing, and structural assessment* of such a chassis, tracing its development from initial CAD conception to final validation through finite element analysis (FEA).

In Section 3.1, this work addresses the 3D modeling stage, carried out using Autodesk Inventor, and outlines the design rationale, imposed constraints, and the spatial arrangement of the electronic components. Particular emphasis is placed on the modular architecture adopted to facilitate both assembly and maintenance of the drone.

Through Section 3.2, this article describes the manufacturing and 3D printing process based on Fused Deposition Modeling (FDM), including slicing strategies, printing profiles, and the assembly sequence of the physical structure.

The structural performance of the chassis is then examined in Section 3.3 using *Finite Element Method (FEM)* simulations. This section defines the applied load conditions, details the mechanical properties of the PETG material, and specifies the failure criteria employed to assess the robustness of the design.

Finally, Section 3.4 present a series of *case studies* together with their corresponding *results analysis*, evaluating the chassis under representative operational scenarios such as hover, maximum thrust, lateral impact, and dynamic manoeuvres.

3.1. CAD Modeling of the Custom Chassis

The three-dimensional modeling stage constitutes a fundamental phase in the chassis development process because it defines the base geometry onto which the drone's various modules will be integrated. Using CAD tools—specifically *Autodesk Inventor*—both the overall structural arrangement and the specific construction details were precisely defined.

Individual part files (`.ipt`) were developed and subsequently assembled into `.iam` assembly files, producing a digital mock-up of the system. This virtual model enables the validation of dimensional compatibility between components and anticipates potential interferences, fastening requirements, and cable routing paths.

This subsection presents the principal design considerations applied during modeling, together with the modular integration philosophy that characterizes the chassis. It also refers to the most relevant structural and electronic elements. It anticipates their functional behavior, which will be evaluated later in the sections dedicated to physical fabrication and structural simulation analysis.

3.1.1. Design Considerations

The 3D design and modeling of the chassis and its components were carried out using *Autodesk Inventor*. This procedure enabled an accurate representation of each part's geometry and its correct mutual interaction within the global system. Part files (`.ipt`) were progressively assembled into `.iam` assemblies using geometric constraints (*constraints*) to ensure alignment, contact, and appropriate relative positioning.

The primary objective of the 3D model is to facilitate the correct placement of electronic and mechanical components within the chassis, enabling secure fixation, optimization of available space and interference assessment. This approach allows a pre-assembly validation that reduces potential integration errors during the real assembly stage.

In Figure 1, the general assembly of the drone is shown, illustrating the layout of the various elements on the modeled chassis. The overall drone frame has a diagonal motor-to-motor distance of 200 mm, and the final assembled weight including the battery is 245 g.

The GPS Module is mounted on the upper plate of the chassis, enclosed within a screwed support that provides mechanical protection and ensures optimal orientation for satellite signal reception. This fastening also reduces the risk of vibration or displacement that could impair its operation. Similarly, the radio receiver (Rx) has been placed on the underside of the upper plate and secured using a custom structure.

The Video Transmitter (VTX) is located on the lower plate of the chassis and is fixed by an additional bracket specifically designed to permit ventilation and to minimize contact with other critical parts. This strategic positioning improves heat dissipation and mitigates potential electromagnetic interference with other modules.

Figure 1. General view of the drone 3D assembly in Autodesk Inventor.

The chassis was designed following a philosophy of modularity and simplified maintenance. To this end, 25 mm aluminum hexagonal standoffs are used to join the upper and lower plates quickly and firmly. This system provides structural stiffness without sacrificing accessibility for maintenance or component replacement.

The FPV camera is mounted on an independent bracket that includes two lateral protective arms whose geometry cushions frontal or lateral impacts. Furthermore, the bracket design allows manual adjustment of the camera tilt angle, which is essential to adapt the view for different flight configurations or conditions.

The drone arms are inserted into a central frame that is fixed to the lower plate using standard M3 fasteners. This frame also houses the Flight Controller (FC), positioned slightly forward on the chassis to shift the center of gravity (CoG) forward. This configuration promotes a small positive pitch attitude in flight, improving forward-flight response. Both the frame and the arms are offset towards the front relative to the longitudinal midplane, consistent with this mass distribution. Additionally, holes have been avoided in the arms themselves to prevent stress concentrations and possible structural weak points that could compromise mechanical integrity.

The main battery is mounted on the upper plate and secured with a Velcro strap that passes through purpose-designed recesses. Electrical connection is provided via an XT30 connector embedded in a cavity on the upper plate to ensure immobility and facilitate quick connection/disconnection.

Both chassis plates incorporate strategically distributed hexagonal cutouts whose dual functions are as follows: (i) to allow passive ventilation of internal components (particularly the VTX); and (ii) to reduce total weight by removing non-functional material without compromising structural integrity.

3.1.2. CAD Design and Component Assembly

The main assembly file (`.iam`) was organized hierarchically to structure the different functional sub-assemblies of the drone. This hierarchy facilitated both the design process and the verification of the complete model. Principal sub-assemblies include the *Core Assembly*, the *Fastening Block*, the *Chassis Assembly* and the *Complete Assembly*. This modular distribution allows logical isolation of components, simplifying editing, review, and technical documentation.

During assembly in the Autodesk Inventor environment, specific geometric constraints (*mate*, *flush*, *insert*, and *angle*) were used to guarantee precise alignment and correct spatial disposition of components. Care was taken to avoid redundant constraints that could produce over-constrained systems, thus ensuring predictable model behavior.

To guarantee the feasibility of physical assembly, systematic collision and interference checks were performed using the CAD software's native tools. Exploded views and sectional cuts were also generated to facilitate inspection of internal critical areas and to support the later generation of assembly documentation.

Dimensional considerations were incorporated from this stage. Functional tolerances were defined in contact and mechanical fastening zones—particularly where sensitive electronic components are inserted or where concentrated loads act, such as at the arm–frame joints. These tolerances are reflected in the technical drawings generated from the assembled model.

The exploded views of the main sub-assemblies, along with the final assembled CAD model, are presented in Figure 2, offering a complete visualization of the UAV's structural configuration.

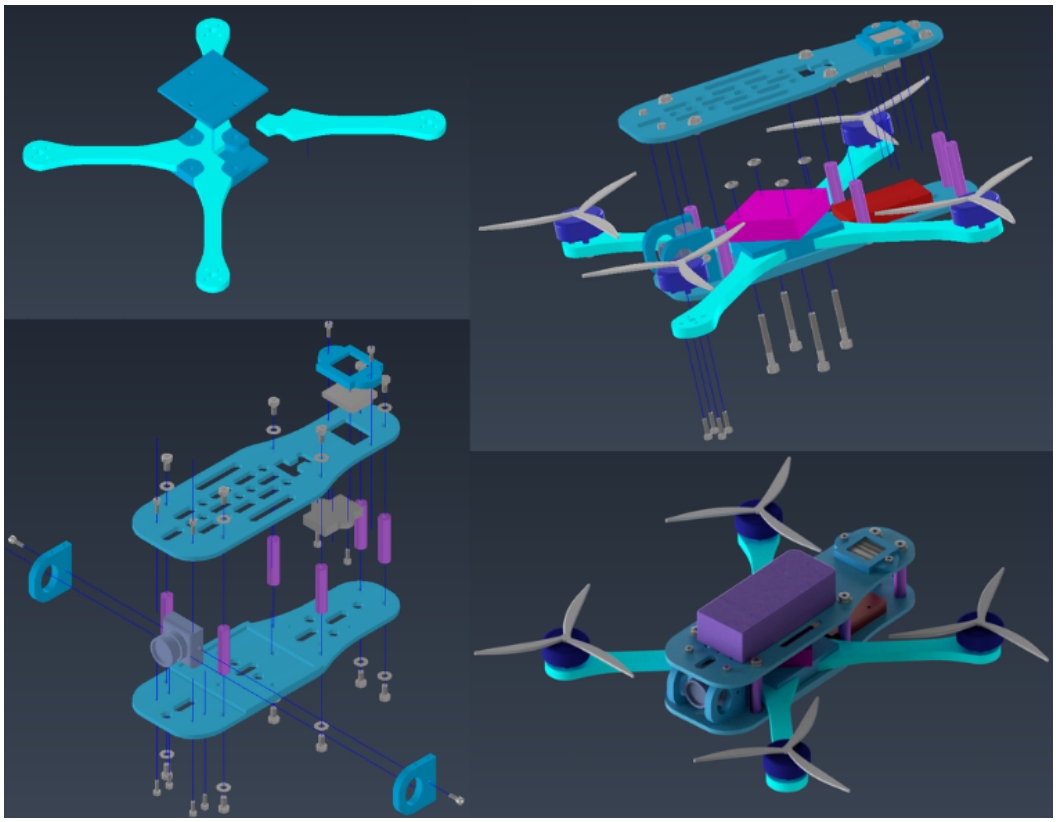

Figure 2. Partial exploded views and final assembly figure.

3.2. Fabrication and 3D Printing via FDM Additive Manufacturing

Additive manufacturing, commonly known as 3D printing, has revolutionized manufacturing processes in recent years. Among the different available technologies, Fused Deposition Modeling (FDM) stands out for its accessibility, versatility, and low cost. This subsection describes the complete fabrication process of a custom drone chassis using FDM 3D printing, covering the preparation of digital files through to the final assembly of the device.

3.2.1. Slicing and Print Profiles

Prior to printing, the digital model must be prepared through a process known as slicing. This procedure divides the three-dimensional model into successive layers, thereby generating the instructions that the printer will follow during fabrication. Additionally, the appropriate selection of print profiles—parameters such as temperature, speed, and material type—is essential to guarantee the quality and strength of the final part. This subsection details the tools and key considerations for efficient slicing and optimal print profile configuration.The main 3D printing parameters used for the fabrication of the arms are summarized in Table 3.

In contrast to the arms, the drone base was designed prioritizing weight reduction without compromising the structural stiffness required to support electronic components. To achieve this, the print profile parameters were adjusted mainly by reducing infill density. This strategy produces a lighter part, reducing material consumption and print time—both critical in UAS design where total weight is a limiting parameter. The main 3D printing parameters used for the fabrication of the base are summarized in Table 4.

Table 3. Principal printing parameters of the profile used for the arms.

No.	Parameter	Value	Description
1	Layer height	0.2 mm	Thickness of each layer. Balance between quality and speed.
2	Line width	0.66 mm	Wider extrusion line to improve strength.
3	Infill density	100%	Solid printing suitable for functional, load-bearing parts.
4	Infill pattern	Grid	Grid pattern for greater structural uniformity.
5	Nozzle temperature	230 °C	Extruder temperature suitable for filaments such as PLA+ or PETG.
6	Bed temperature	70 °C	Improves first-layer adhesion and reduces warping.
7	Print speed	60 mm/s	Medium speed—compromise between quality and time.
8	Wall speed	30 mm/s	Half the general speed for better surface finish.
9	Initial layer speed	15 mm/s	Reduced speed to ensure good base adhesion.
10	Cooling	Enabled	Layer fan active for rapid solidification.
11	Bed adhesion	None	No brim, raft, or skirt used.
12	Supports	No	The part does not require support structures.

Table 4. Main printing parameters used for the drone base.

No.	Parameter	Value	Description
1	Layer height	0.2 mm	Good balance between detail and printing speed.
2	Line width	0.66 mm	Consistent with the rest of the chassis to maintain strength.
3	Infill density	40%	Partial infill to lighten the base plate.
4	Infill pattern	Grid	Balanced distribution of material for stiffness.
5	Nozzle temperature	230 °C	Adjusted for good interlayer adhesion.
6	Bed temperature	70 °C	Guarantees good initial adhesion.
7	Print speed	60 mm/s	Standard printing speed.
8	Wall speed	30 mm/s	Reduces visible edge imperfections.
9	Initial layer speed	15 mm/s	Facilitates first-layer adhesion.
10	Cooling	Enabled	Improves surface finish and prevents distortions.
11	Bed adhesion	None	Adequate without additional aids.
12	Supports	No	Geometry optimized to print without supports.

The remainder of the chassis components were printed following a strategy similar to that used for the base, employing moderate infill density and optimized parameters to reduce total weight without compromising functionality or structural integrity. This consistency in print configuration ensures homogeneous mechanical behavior of the assembled frame and greater efficiency in the fabrication process.

3.2.2. Assembly and Drone Construction

Once all parts composing the chassis and the structural elements have been printed, the assembly and construction phase of the drone is initiated. This stage is crucial, as it is where the electronic components responsible for the system's overall operation are integrated.

The process begins with the mechanical completion of the printed chassis. The total weight of the assembled frame is 78 g. A general view of the final printed assembly is shown in Figure 3, which illustrates the robustness of the printed structure and the quality of the FDM process prior to the integration of electronic subsystems.

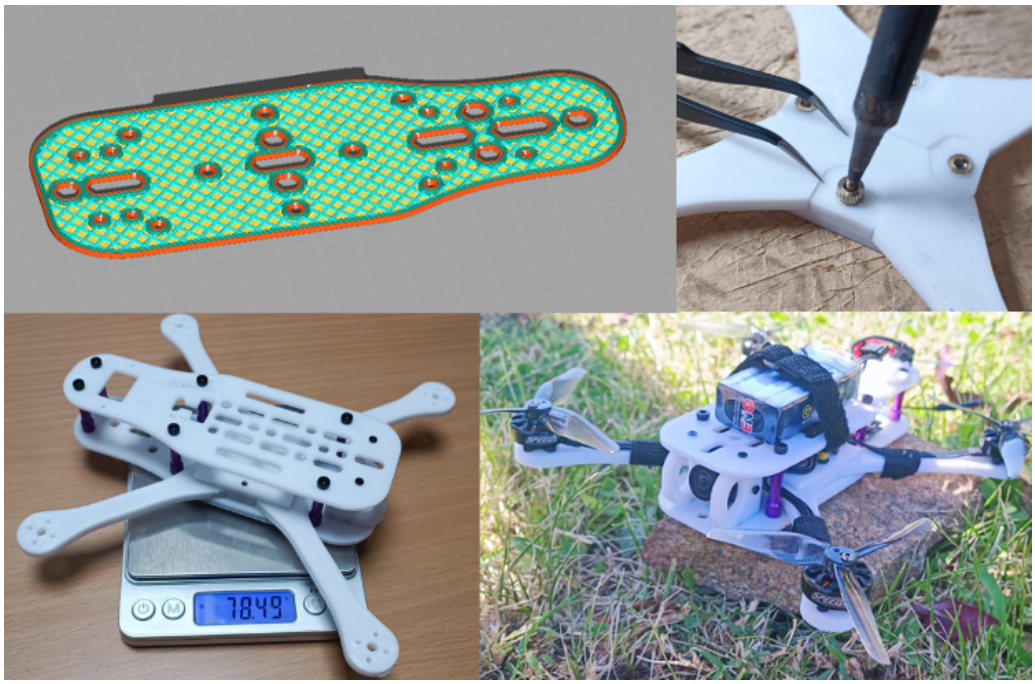

Figure 3. Steps of the fabrication process for the UAV structure.

After the successful fabrication and verification of the printed chassis, the next step consists of completing the drone assembly by integrating the electronic subsystems. This phase is crucial, since it transforms the printed structure into a functional aerial platform.

The process begins with the installation of the All-in-One Flight Controller (Flight Controller AIO), which centralizes functions such as stabilization, motor control, sensor reading, and command processing. The radio frequency receiver is then installed to capture the pilot's control input, followed by the GPS Module required for advanced navigation, positioning, and Return-to-Home functions.

Subsequently, the Video Transmitter (VTX) is installed to provide the real-time video feed from the onboard camera to FPV goggles or an operator's display. Finally, the motors are fixed to the arms and connected to the electronic speed controllers (ESCs), which may either be integrated into the AIO board or implemented externally.

All electronic connections were carried out in accordance with the wiring specifications provided by the manufacturers of each component, including the Flight Controller, receiver, VTX, and GPS. Following these guidelines ensured system compatibility and reduced the risk of faulty wiring.

During this phase, the use of specific tools—precision screwdrivers, a fine-tip soldering iron, a multi-meter, and anti-static tweezers—is recommended. It is also essential to pay attention to cable routing and cleanliness, ensuring solid connections protected against vibration to guarantee optimal performance in flight and to minimize the risk of failures during operation. The fully assembled drone can be seen at Figure 3.

3.3. Structural Analysis of the Chassis by Finite Element Simulation (FEM)

The objective of this work is to analyze the mechanical behavior of the primary structure of a quad-X configuration drone chassis, focusing on the cross-shaped structural element formed by the arms and the central frame that joins them. This part is responsible for transmitting aerodynamic loads and impacts. The remainder of the frame—comprising the platforms where components such as the battery and controllers are mounted—is bolted in a sandwich arrangement over this cross but does not contribute significantly to the load-bearing function. This supporting platform has therefore been excluded from

the model to simplify and accelerate calculations without compromising the validity of the analysis.

The analysis was performed using the Finite Element Analysis (FEA) method. FEA allows subdivision of a complex geometry into simpler elements where equilibrium equations are solved to obtain stress, strain, and displacement fields. This methodology is especially suitable for complex geometries, anisotropic materials, such as 3D-printed plastics, and variable loading conditions, as in the case of a drone [21,22]. FEA enables the prediction of material behavior prior to manufacture, reducing test costs and development time [23].

3.3.1. Model and General Conditions

The chassis cross was modeled as an `.iam` assembly with motion constraints applied to its components—it was effectively treated as a solid assembly whose mechanical properties correspond to PETG. The following simplifications were considered:

- The model excludes motors and electronics, which are represented as equivalent concentrated loads.
- The mesh is refined in critical regions: joints, arm ends and the base of the frame, following best practices in FEM with Inventor Nastran [24,25].

3.3.2. PETG Material Properties

FDM-printed plastics exhibit anisotropic behavior; mechanical properties vary with build orientation. For example, studies show that the "Young's modulus" and "tensile strength" differ significantly between XY and Z directions [26–28]. Likewise, process parameters such as "extrusion temperature, printing speed, layer height, and infill density" strongly affect the mechanical performance [28]. Finite element modeling and homogenization techniques have also been applied to derive effective stiffness matrices, demonstrating that PETG can be described as a "transversely isotropic material" [27,29]. Other works focus on "reinforced PETG composites," investigating tensile, flexural, and compressive behavior, with validation by both simulation and experiments [30]. More recently, reviews emphasize the influence of parameters such as "nozzle temperature, bed temperature, speed, layer height, and infill density" on mechanical strength [31].

A summary of the material properties used is presented in Table 5.

Table 5. Minimum mechanical properties for PETG printed by FDM used in the analysis.

Property	Plane XY	Plane Z
Young's modulus E [MPa]	2100	1600
Tensile strength [MPa]	50	35
Yield strength (0.2% offset) [MPa]	40	25
Elongation at break [%]	15	5
Density [kg/m^3]	1270	
Poisson's ratio	0.38	
Plastic behavior	Elastic—perfectly plastic	

3.3.3. Failure Criteria Employed

Three methods were employed to evaluate the potential for structural failure depending on the loading type and analysis objective:

- **Von Mises criterion:** useful to predict yielding in ductile materials. Applied mainly under multi-axial stress states such as impacts or manoeuvres with acceleration [32].
- **Maximum principal stress criterion:** more conservative, used in uniaxial loading conditions or to verify areas with high stress concentrations [32].

- **Maximum strain criterion:** particularly relevant for anisotropic materials like 3D-printed plastics, where excessive deformation in the Z-direction can cause layer delamination [33–35].

The component is considered to have failed if the following occur:

- The Von Mises stress exceeds the material's yield strength in the corresponding direction [32].
- The strain in the Z-direction surpasses 5% [33,34].

3.4. Study Cases

The structural evaluation of the drone chassis was conducted under representative flight conditions using the Finite Element Method (FEM). Different load cases were simulated in order to determine the structural integrity, stress distribution, and deformation of the printed frame. The first case corresponds to hovering flight, which establishes a reference baseline for subsequent analyses under more demanding manoeuvres.

3.4.1. Hovering Flight Analysis

In this scenario, the drone is simulated under steady hovering conditions, where the lift force generated by the rotors exactly balances the vehicle's weight. This represents the baseline structural load case and serves as a reference for more complex operational scenarios. The load distribution is assumed to be uniform across the four arms, enabling a straightforward evaluation of stresses, displacements, and the safety factor using the Finite Element Method (FEM).

- **FEM Study** For this condition, the drone's total mass of 250 g is evenly distributed among the four arms:

$$\text{Mass per arm} = \frac{\text{Total mass}}{4} = \frac{250\,\text{g}}{4} = 62.5\,\text{g} = 0.0625\,\text{kg} \tag{1}$$

Applying Newton's second law, the equivalent force acting on each arm is:

$$F = m \cdot g = 0.0625\,\text{kg} \cdot 9.81\,\text{m/s}^2 = 0.613\,\text{N} \tag{2}$$

The total force generated by the four rotors is therefore:

$$F_{\text{total}} = 4 \cdot 0.613\,\text{N} = 2.452\,\text{N} \tag{3}$$

The resulting vertical acceleration is:

$$a = \frac{F_{\text{total}}}{m_{\text{drone}}} = \frac{2.452}{0.250} = 9.81\,\text{m/s}^2 \tag{4}$$

$$a_{\text{G}} = \frac{a}{g} = \frac{9.81}{9.81} = 1.0G \tag{5}$$

This case corresponds to a hovering flight condition with a vertical acceleration of 1.0 G representing static lift equilibrium. The parameters applied in the simulation are summarized in Table 6.

The PETG used for the 3D-printed chassis has an approximate yield strength of:

$$\sigma_{\text{limit}} = 40\,\text{MPa} \tag{6}$$

The maximum Von Mises stress obtained in this case is:

$$\sigma_{\text{VM}} = 0.6973\,\text{MPa} \tag{7}$$

Table 6. Simulation conditions for hovering flight.

Parameter	Value
Total drone mass	250 g
Load per arm	0.613 N
Total force	2.452 N
Total acceleration	9.81 m/s^2
Total acceleration (G)	1.0 G
Load direction	Vertical upward
Constraints	Chassis base fixed
Analysis type	Linear static
Failure criterion	Von Mises (maximum stress)
Mesh size	0.1 mm

The resulting safety factor is:

$$\mathrm{SF} = \frac{\sigma_{\mathrm{limit}}}{\sigma_{\mathrm{VM}}} = \frac{40}{0.6973} \approx 57.36 \tag{8}$$

This indicates that, under normal hovering conditions, the structure operates far below its material limit, with a very wide safety margin (Table 7).

Table 7. Structural results during hovering flight.

Magnitude	Minimum	Maximum
Von Mises stress	0.00056 MPa	0.70 MPa
First principal stress	−0.05 MPa	0.80 MPa
Third principal stress	−0.76 MPa	0.11 MPa
Total displacement	0 mm	0.234 mm
Safety factor	57.00	N/A

- **Results Analysis**

Figure 4 shows the distribution of Von Mises stresses, with maximum concentrations at the arm–chassis junction. Figure 5 indicates that the maximum displacement (0.234 mm) occurs at the free ends of the arms.

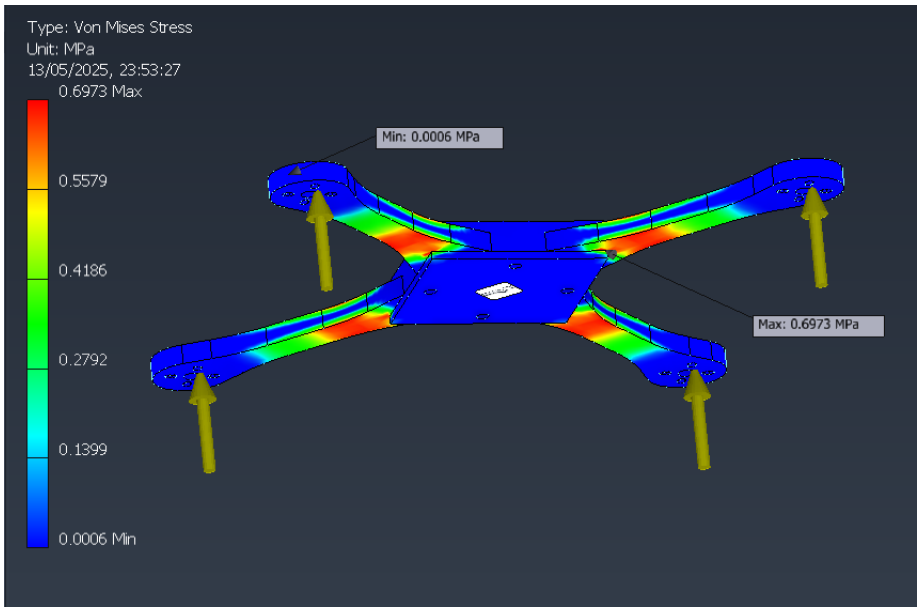

Figure 4. Von Mises stress distribution during hovering flight.

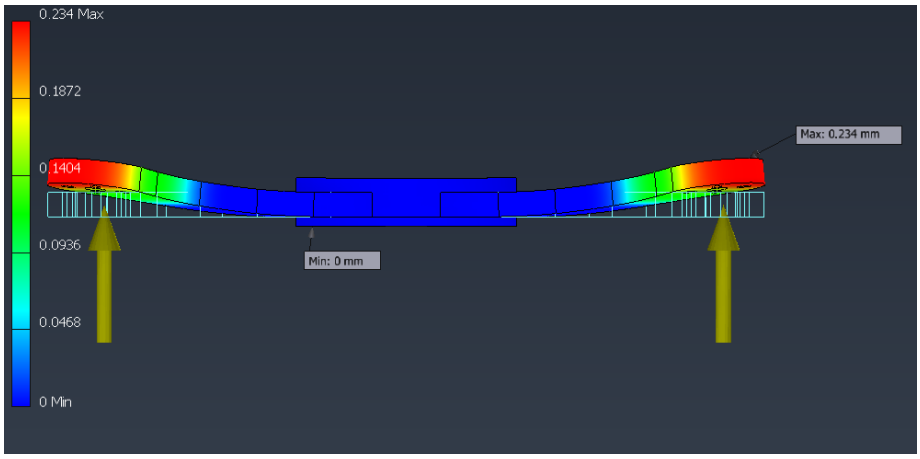

Figure 5. Total displacement map during hovering flight.

- **Simplified beam model validation**

To validate the numerical simulations, a simplified theoretical model was implemented, representing the drone arm as a cantilever beam with an equivalent rectangular cross-section. This approximation provides a first-order estimation of stresses and displacements and allows comparison with the results obtained from FEM simulations of both the individual arm and the fully assembled structure.

Model data:

- Cantilever beam with rectangular cross-section
- Length: $L = 70$ mm
- Width: $b = 10$ mm
- Height: $h = 5$ mm
- Point load: $F = 0.625$ N applied at the free end in $+Z$ direction
- Young's modulus (PETG): $E = 2.1 \times 10^9$ Pa

Calculations:

$$I = \frac{bh^3}{12} = 1.0417 \times 10^{-10}\ \text{m}^4$$

$$\delta_{\max} = \frac{FL^3}{3EI} \approx 0.327\ \text{mm}$$

$$M_{\max} = F \cdot L = 0.04375\ \text{Nm}$$

$$\sigma_{\max} = \frac{M_{\max} \cdot c}{I} = 1.05\ \text{MPa}$$

$$\sigma_{\text{vm}} = |\sigma| = 1.05\ \text{MPa}$$

Comparison of results: To compare the simplified model against numerical simulations, a load of 0.625 N was applied, corresponding to the thrust generated by a single motor under hovering conditions. Table 8 summarizes the results.

Table 8. Comparison of Von Mises stresses and maximum displacements under hovering load (0.625 N).

Case	Von Mises Stress (MPa)	Max. Displacement (mm)
Simplified cantilever beam	1.05	0.327
Individual arm (CAD model)	0.77	0.3266
Assembled arm	0.69	0.234

The simplified beam model provides a conservative estimate of stresses and displacements. As expected, the inclusion of the actual geometry and the structural connection of

the arm to the chassis increases stiffness, thereby reducing both stresses and deflections under identical load conditions. The difference between the individual arm and the assembled model is mainly attributed to the boundary conditions: in the assembled configuration, the frame corner acts as a stiffer constraint, reducing the effective bending moment.

The results obtained from the mechanical and static analyses confirm the validity of the PETG model under the expected operating conditions. The relatively low applied loads, the limited Von Mises stresses, and the small displacements observed indicate that the structure operates well within safe limits, thus validating the chosen manufacturing process and material assumptions. Consequently, these findings support the feasibility of future production using carbon fiber composites, which, due to their significantly higher stiffness and strength, would further enhance the structural performance and reliability of the final design.

The FEM results for the individual arm under hovering load are shown in Figures 6 and 7.

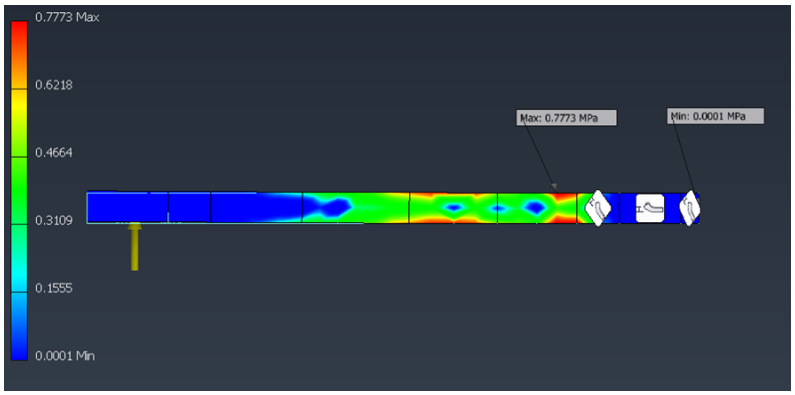

Figure 6. Von Mises stress distribution in the individual drone arm under a 0.625 N load.

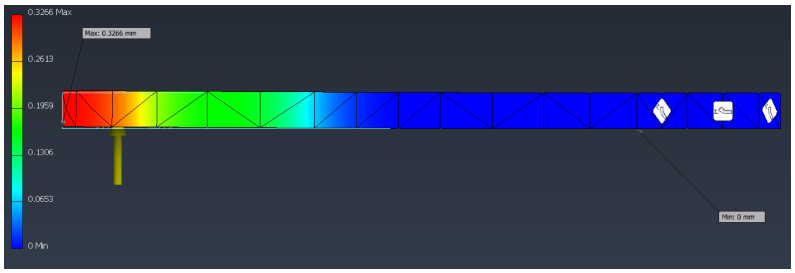

Figure 7. Displacement field in the individual drone arm under a 0.625 N load.

3.4.2. FEM Structural Study at Maximum Motor Thrust (10.4 G)

This analysis evaluates the structural behavior of the 3D-printed frame under the most demanding loading scenario: the maximum thrust is delivered by the motors at full throttle. Unlike the hovering condition, this case does not represent a realistic steady flight state but rather an idealized vertical acceleration situation, introduced to assess the structural safety margins of the chassis under extreme conditions.

- **FEM Study**

When the motors operate at 100% throttle, each motor produces a thrust of approximately 650 g (647 g according to the manufacturer's data sheet). The model assumes that the total thrust acts directly on the arms, while the central base of the frame is fully constrained. This conservative simplification allows a direct evaluation of the maximum stresses and displacements that the structure could undergo. A summary of the simulation conditions can be found in Table 9.

$$\text{Thrust per arm} = 650\,\text{g} = 0.650\,\text{kg}$$

$$F = m \cdot g = 0.650\,\text{kg} \cdot 9.81\,\text{m/s}^2 = 6.38\,\text{N}$$

$$F_{\text{total}} = 4 \cdot 6.38\,\text{N} = 25.51\,\text{N}$$

$$a = \frac{F_{\text{total}}}{m_{\text{drone}}} = \frac{25.51}{0.250} \approx 102.02\,\text{m/s}^2 \approx 10.4\,G$$

Table 9. Simulation conditions under maximum motor thrust.

Parameter	Value
Thrust per motor	650 g
Force per arm	6.38 N
Total force	25.51 N
Drone mass	250 g
Total acceleration	102.02 m/s^2
Acceleration (G)	10.4 G
Load direction	Vertical upward
Boundary condition	Frame base fixed
Analysis type	Linear static
Failure criterion	Von Mises (maximum stress)
Mesh size	0.1 mm

- **Results**

From the FEM simulation, the maximum Von Mises stress was observed at 7.25 MPa, concentrated near the arm–frame junction (Figure 8). The maximum displacement, 2.43 mm, occurs at the free end of the arms (Figure 9). Considering the PETG yield strength of 40 MPa, the safety factor is:

$$\text{SF} = \frac{\sigma_{\text{yield}}}{\sigma_{\text{VM}}} = \frac{40}{7.25} \approx 5.52$$

A summary of the simulation results can be found in Table 10.

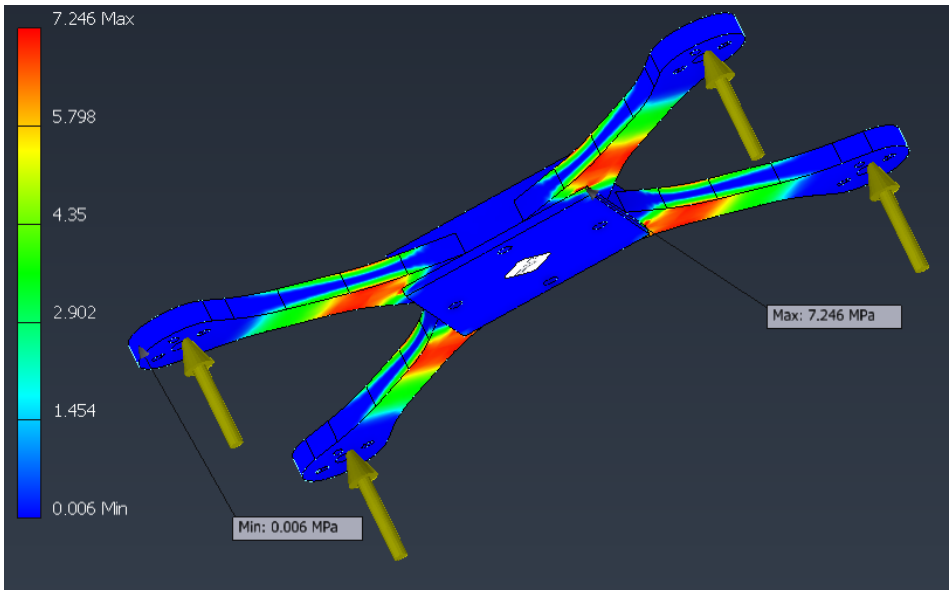

Figure 8. Von Mises stress distribution under maximum thrust. Stress concentration is observed at the arm–frame junction.

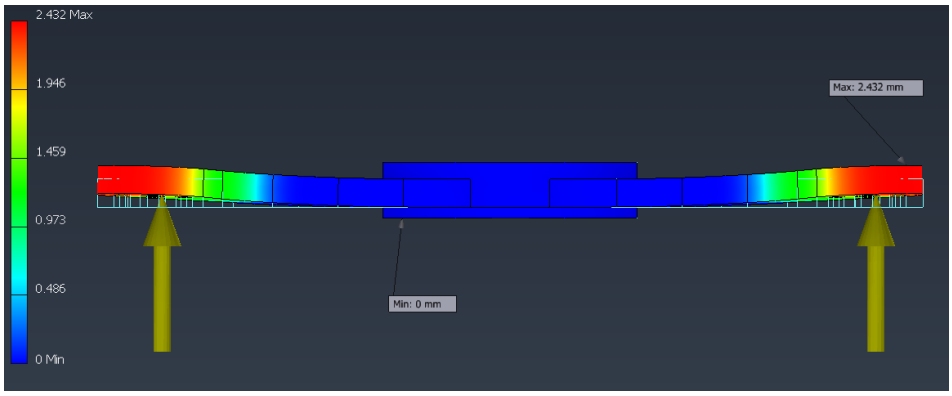

Figure 9. Total displacement map under maximum thrust. Maximum displacement of 2.43 mm occurs at the free ends of the arms.

Table 10. Structural results under maximum motor thrust.

Magnitude	Min	Max
Von Mises stress	0.0059 MPa	7.25 MPa
First Principal stress	−0.52 MPa	8.34 MPa
Third Principal stress	−7.88 MPa	1.19 MPa
Total displacement	0 mm	2.43 mm
Safety factor	5.52	N/A

- **Simplified beam model validation**

The simplified cantilever beam model was tested under the same extreme condition of 6.38 N applied at the free end. The objective is to validate the order of magnitude of stresses and displacements compared with the CAD-based FEM simulation.

Model data:

- Cantilever beam with rectangular cross-section.
- Length: $L = 70$ mm.
- Width: $b = 10$ mm.
- Height: $h = 5$ mm.
- Point load: $F = 6.38$ N in $+Z$ direction.
- Young's modulus (PETG): $E = 2.1 \times 10^9$ Pa.

Calculations:

$$I = \frac{bh^3}{12} = 1.0417 \times 10^{-10}\ \text{m}^4$$

$$\delta_{\max} = \frac{FL^3}{3EI} \approx 3.34\ \text{mm}$$

$$M_{\max} = F \cdot L = 0.4466\ \text{Nm}$$

$$\sigma_{\max} = \frac{M_{\max} \cdot c}{I} \approx 10.71\ \text{MPa}$$

$$\sigma_{\text{vm}} = |\sigma| = 10.71\ \text{MPa}$$

The comparison under high-load conditions is summarized in Table 11.

As in the hovering case, the simplified model predicts slightly higher stresses than the CAD simulations. This difference is explained by the stiffening features of the real arm geometry, which help reduce stresses under the same load.The Von Mises stress and displacement distributions are shown in Figures 10 and 11, respectively.

Table 11. Comparison of Von Mises stress and maximum displacements under elevated load (6.38 N).

Case Analyzed	Von Mises Stress (MPa)	Max Displacement (mm)
Simplified beam (theoretical model)	10.71	3.34
Individual arm (CAD model)	7.93	3.34
Arm in full drone assembly	7.25	2.43

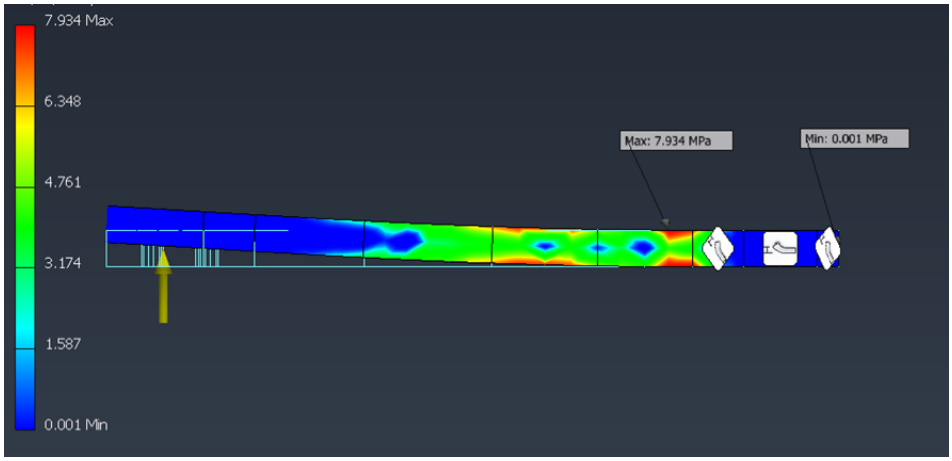

Figure 10. Von Mises Stress analysis of a single drone arm under 6.38 N load.

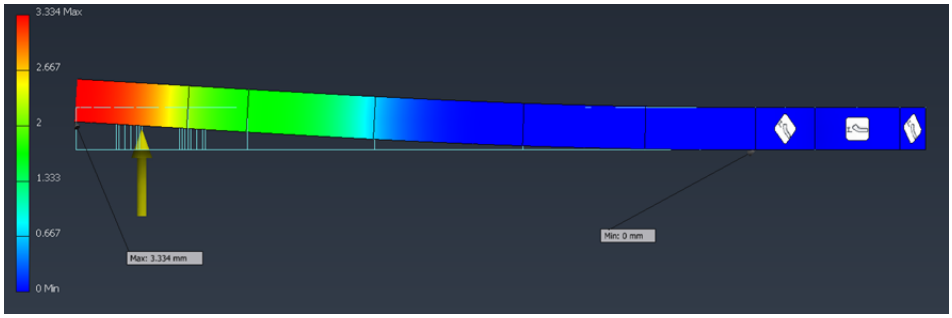

Figure 11. Displacement analysis of a single drone arm under 6.38 N load.

- **Comparative Results PETG–Carbon Fiber**

The FEM simulations for PETG and carbon fiber under the same loading conditions reveal substantial differences in mechanical performance, primarily due to the superior stiffness and strength of the carbon fiber material, while the stress levels remain similar between both cases, the displacement and safety factor show remarkable improvements when using carbon fiber. Table 12 summarizes the comparison between the analyzed materials.

Considering the carbon fiber yield strength of 300 MPa, the safety factor is calculated as follows:

$$\mathrm{SF} = \frac{\sigma_{\mathrm{yield}}}{\sigma_{\mathrm{VM}}} = \frac{300}{7.25} = 41.38 \tag{9}$$

The maximum Von Mises stress remains constant at 7.25 MPa for both materials, as the geometry and load conditions are identical. However, the maximum displacement decreases from 2.43 mm with PETG to only 0.038 mm with carbon fiber, representing a drastic improvement in stiffness and deformation control.

Table 12. Comparison of structural results between PETG and carbon fiber under maximum thrust.

Magnitude	PETG	Carbon Fiber
Von Mises stress (max)	7.25 MPa	7.25 MPa
First Principal stress (max)	8.34 MPa	8.38 MPa
Third Principal stress (min)	−7.88 MPa	−7.91 MPa
Total displacement (max)	2.43 mm	0.038 mm
Yield strength	40 MPa	300 MPa
Safety factor	5.52	41.38

The safety factor increases from 5.52 to 41.38 due to the significantly higher yield strength of carbon fiber (300 MPa vs. 40 MPa). These results demonstrate that, although both materials experience similar stress distributions, the structural response of the carbon fiber model is far superior in terms of rigidity and safety margin. As shown in Figure 12, the deformation in the carbon fiber structure is minimal compared to the PETG case, while Figure 13 highlights the distribution of principal stresses, confirming similar stress patterns but significantly reduced strain magnitudes.

In conclusion, replacing PETG with carbon fiber substantially enhances the structure's mechanical performance, reducing deformation by more than 98% and increasing safety by a factor of approximately 7.5, confirming carbon fiber as a more suitable material for high-performance structural applications.

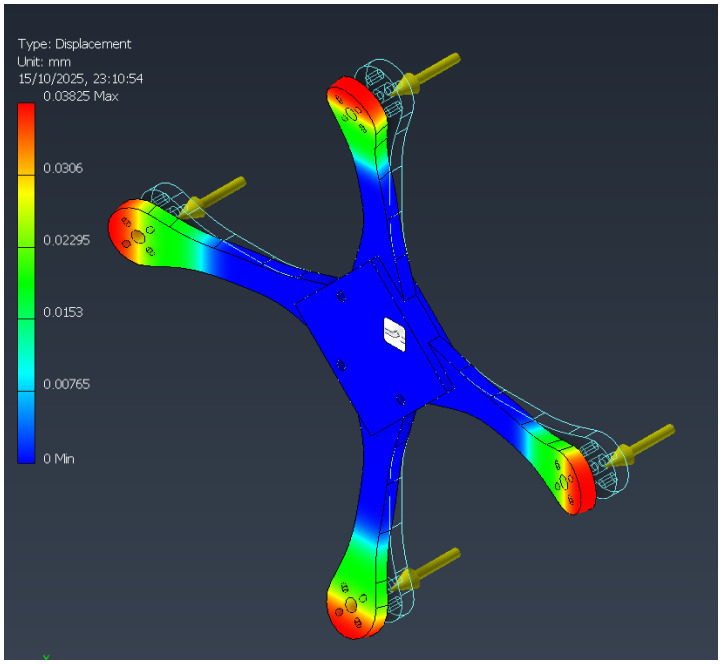

Figure 12. Total displacement distribution for the carbon fiber structure under maximum thrust. Maximum displacement of 0.038 mm occurs at the free end of the arms.

Experimental validation

To validate the numerical FEM results, a preliminary experimental test was performed using a single arm segment of the drone frame. The objective of this test was not to obtain statistically representative data, but rather to verify the order of magnitude of the deformation predicted by the simulations under a controlled static load. The arm was rigidly fixed at one end, replicating the boundary conditions used in the FEM analysis, setup can be observe in Figure 14. A static punctual load equivalent to 625 was applied at the free end, corresponding to a force as follows:

$$F = m \cdot g = 0.625\,\text{kg} \times 9.81\,\text{m/s}^2 = 6.13\,\text{N} \tag{10}$$

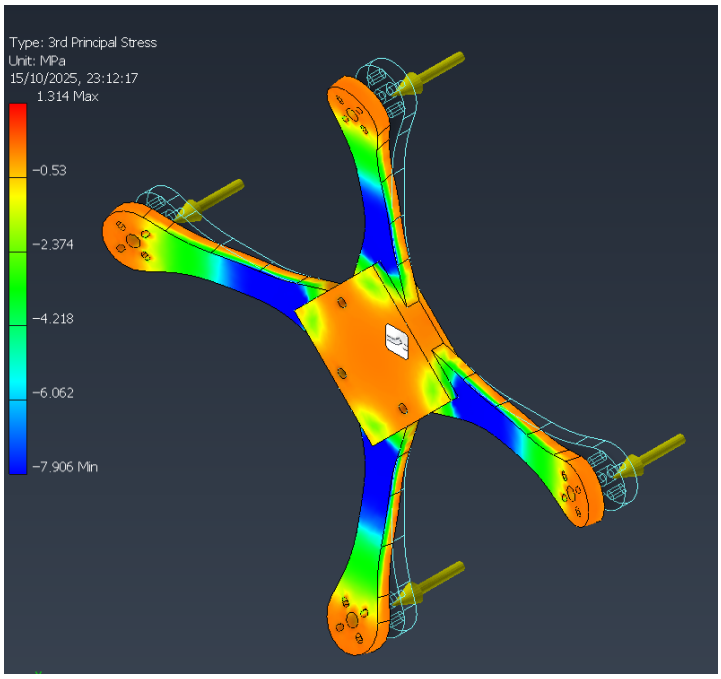

Figure 13. Third principal stress distribution in the carbon fiber model under maximum thrust, showing compression zones near the arm–frame junction.

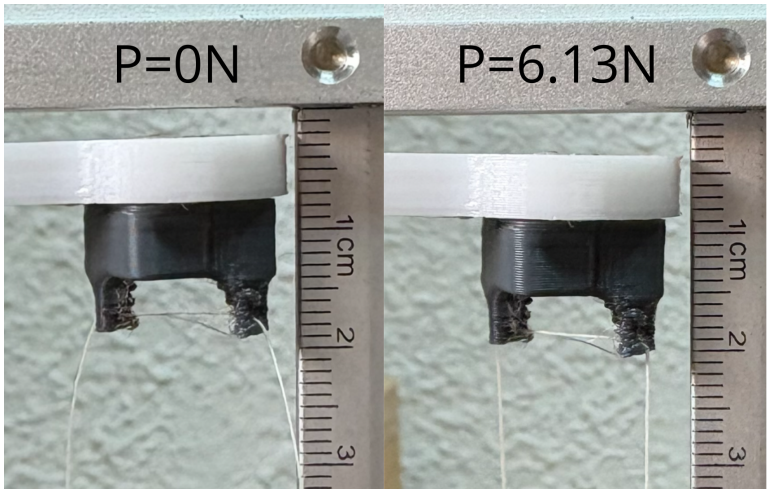

Figure 14. Deformation test.

This value represents the load generated by the arm under an acceleration of approximately 10 G, as simulated in the maximum thrust FEM scenario. For practical implementation, a physical weight of 625 g was suspended from the tip of the printed arm to reproduce the equivalent vertical force.

The resulting vertical displacement was measured manually with a precision of 1 mm. Due to the small magnitude of deformation and the absence of dedicated strain measurement instrumentation (e.g., LVDT or digital displacement sensors), the obtained value represents an approximate observation.

The measured displacement was approximately 1.8 mm, compared with the 3.34 mm predicted by the FEM simulation under the same loading and boundary conditions. This difference is primarily due to the intentionally conservative nature of the FEM analysis, in which the PETG material properties were underestimated (yield strength set to 40 MPa) to ensure a safety margin against printing defects, local stress risers, or interlayer weaknesses.

This conservative modeling approach was chosen to guarantee that, if the simulated model remains within safe limits under these restrictive assumptions, the real printed prototype will also perform safely under actual conditions. Thus, the FEM model acts as a lower-bound validation of structural integrity. Table 13 summarizes the experimental results of the single-arm setup.

Table 13. Experimental validation of a single arm under static load equivalent to 625 g (6.13 N), corresponding to a 10 G acceleration.

Sample	Applied Load (N)	Measured Disp. (mm)	FEM Disp. (mm)	Error (%)
1	6.13	1.8	3.34	46.1

Given the limited precision of the setup and the absence of strain instrumentation, this test should be interpreted only as a qualitative validation confirming that the experimental and numerical deformations are of the same order of magnitude. The results support the validity of the conservative FEM model and demonstrate that the printed structure operates safely within the predicted elastic range.

In summary, this preliminary single-arm static test supports the general validity of the FEM approach while highlighting the need for future tests using precise displacement sensors and multiple samples to improve quantitative correlation.

3.4.3. Structural Response to Lateral Impact at the Arm Tip (40 km/h)

The purpose of this simulation is to study the structural behavior of the drone when it impacts a rigid object (representing a tree) at a speed of 40 km/h or 11 m/s. The collision occurs at the tip of one of the drone's arms, which allows the analysis of the localized response in the structurally most critical area during a crash.

- **Analysis Setup**

The simulation is configured as a nonlinear transient dynamic response with large displacements enabled (`PARAM, LGDISP, 1`). Rayleigh damping coefficients are applied ($\alpha = 1.0 \times 10^{-3}$, $\beta = 1.0 \times 10^{-3}$) to model internal energy dissipation.

The integration step is 1×10^{-6} s, with 1000 iterations per step, and a total duration of 0.01 s. This ensures high temporal resolution of the impact response.

A summary of the main parameters is presented in Table 14.

Table 14. Main parameters used in the analysis.

Analysis type	SOL 129—Nonlinear transient response
Large displacements	Enabled (`PARAM, LGDISP, 1`)
Units	International System (m, kg, s)—`PARAM, UNITS, M`
Rayleigh damping	$\alpha = 1.0 \times 10^{-3}$, $\beta = 1.0 \times 10^{-3}$
Material	PETG: $E = 2.1 \times 10^3$ MPa, $\nu = 0.36$, $\rho = 1270$ kg/m^3
Initial velocity	11 m/s through initial conditions (`IC`)
Collision	Against rigid cylinder (tree), without penetration
External forces	Force of 2.5 N at the base in -Z direction (drone weight of 250 g) and four forces of 0.625 N at the motors in +Z direction (lift)
Integration parameters	Time step: 1×10^{-6} s; iterations: 1000; duration: 0.01 s

To properly characterize the system's response during and after the impact, multiple output variables were enabled, as detailed in Table 15. These allow evaluation of the most relevant physical magnitudes such as displacements, stresses, and internal forces.

Table 15. Physical variables extracted during the analysis.

Variable	Configured Output
Nodal displacement	`DISPLACEMENT(PLOT) = ALL`
Velocity	`VELOCITY(PLOT) = ALL`
Acceleration	`ACCELERATION(PLOT) = ALL`
Corner stress	`STRESS(PLOT,CORNER) = ALL`
Corner strain	`STRAIN(PLOT,CORNER) = ALL`
Internal forces	`FORCE(PLOT) = ALL`

- **FEM Study**

For the simulation, Inventor software 2025 in the Nastran environment is used, which enables transient testing. The model assembly and the meshed drone, composed of triangular elements refined in the impact region, are shown in Figure 15. The tree is represented by a meshed cylinder with rigid properties and completely constrained motion. The adaptive mesh, with higher density in the impact zone, ensures adequate spatial resolution of stresses. A detailed view is shown in Figure 16, where the increase in nodes on the arm under study can be observed, especially on the impact surface.

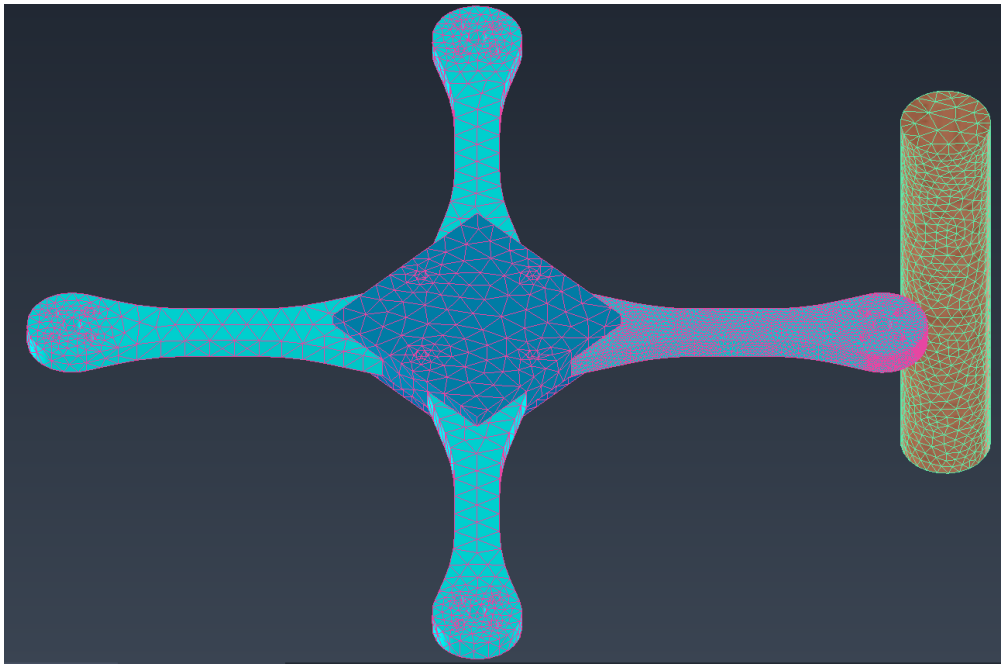

Figure 15. Meshed drone model in Inventor Nastran, with boundary and contact conditions against a rigid cylinder.

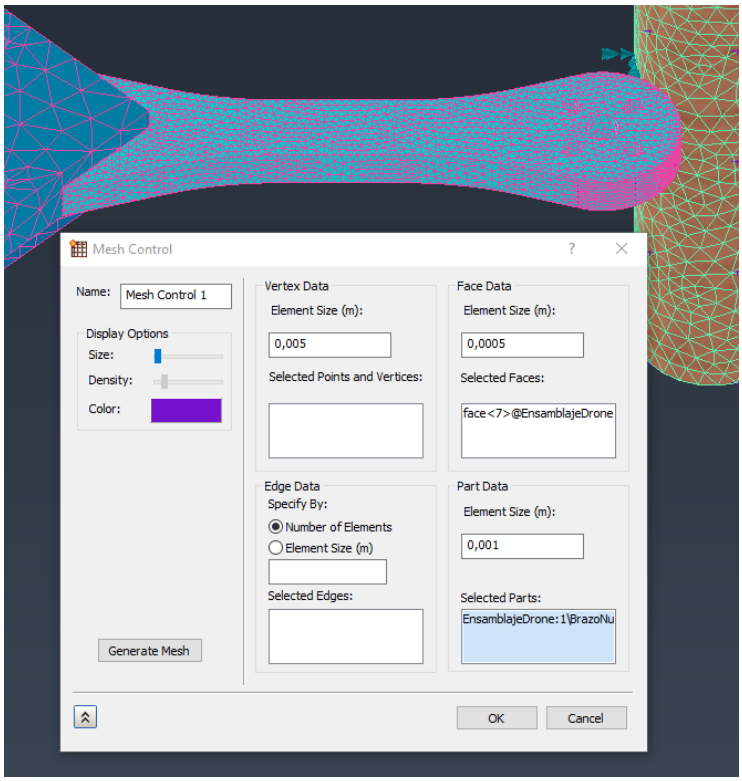

Figure 16. Detail of the adaptive meshing.

The contact between both geometries is defined by non-penetration collision conditions through a boundary contact condition between the arm face and the cylinder simulating the tree, as shown in Figure 17. The boundary conditions ensure the following:

- **Type of penetration:** `symmetric contact`—both surfaces (drone and tree) act interchangeably as master or slave surfaces, improving numerical stability and contact detection accuracy.
- **Stiffness factor:** `1`—maintains physical accuracy without artificial rebounds or numerical penetrations.
- **Coefficient of friction:** `0`—friction neglected due to the short collision time and dominance of normal forces.
- **Penetration Surface Offset:** `0 m`—accurate meshing and alignment require no offset.
- **Max activation distance:** enabled (automatic mode)—the solver determines activation distance dynamically to avoid false contacts.

The details of the applied forces can be seen in Figure 18. The thrust of the motors is simulated by red loads of 0.625 N, the total weight of 250 g by the white load at the bottom of the chassis, and the 11 m/s displacement by green velocity-type loads. The fixed supports of the trunk can also be observed, keeping it immobile.

Finally, the set of boundary conditions (`SPC = 1`) properly restricts the degrees of freedom not involved in the collision. The nonlinear controlled time step (`TSTEPNL = 1`) ensures numerical stability in the transient domain. This configuration provides an accurate and realistic representation of the drone's mechanical behavior during impact, enabling the identification of potential structural failures and critical damage zones.

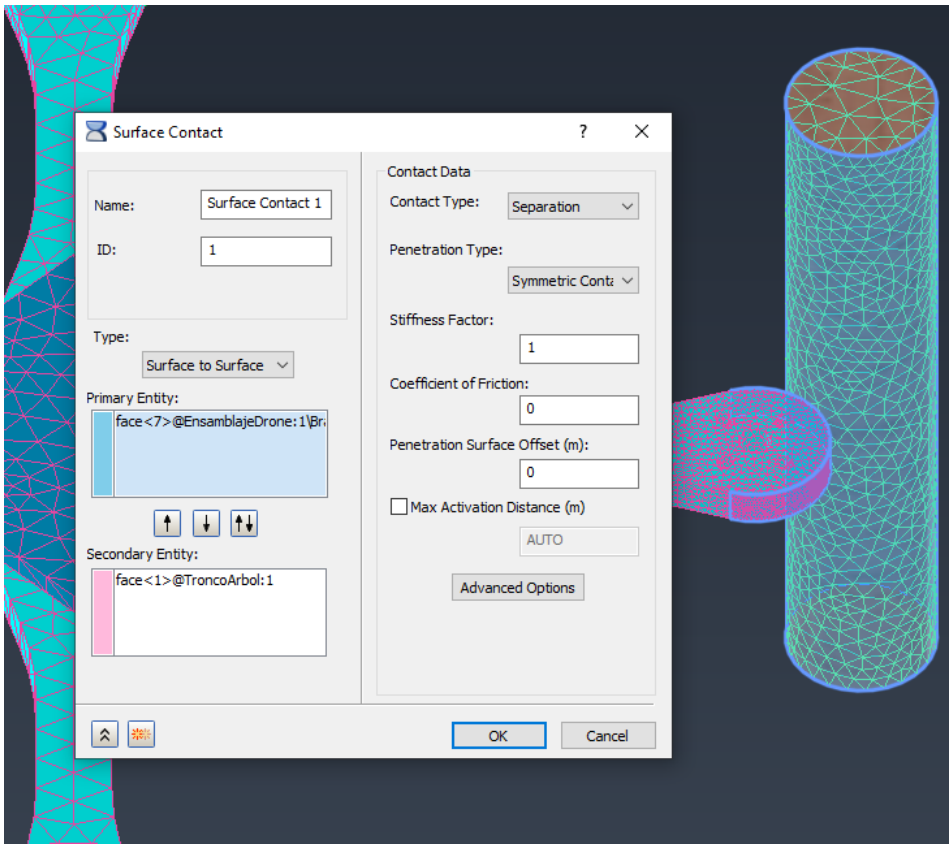

Figure 17. Boundary conditions between the drone's arm and the cylinder.

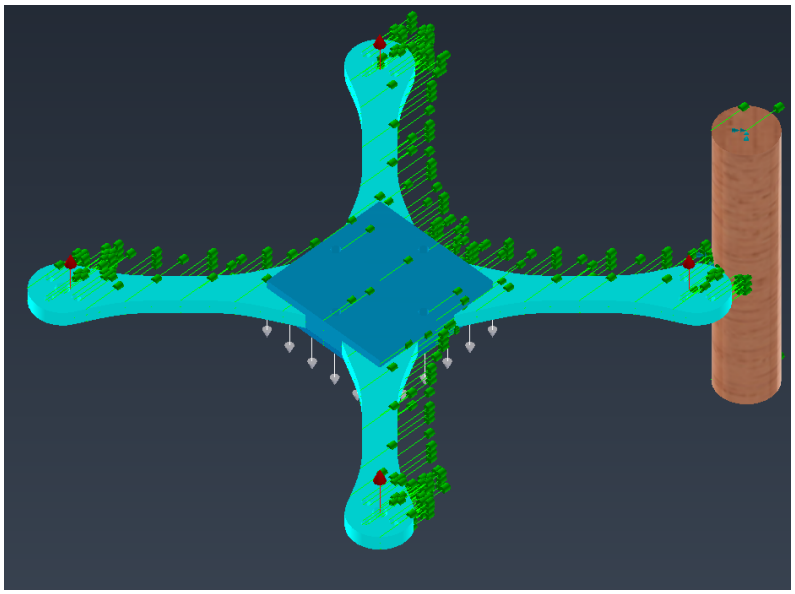

Figure 18. Loads applied to the model.

- **Results**

Two simulations were performed to evaluate the structural response of the drone's frame during the collision: the first at $t = 0.01$ s, corresponding to the initial impact, and the second at $t = 1$ s, to analyze subsequent energy absorption and redistribution.

At $t = 0.01$ s, the stress distribution shown in Figure 19 indicates that the most loaded area coincides with a joint node, an artificial stress concentration caused by mesh discretization (see Figure 20), reaching a maximum value of 29.68 MPa. The diagonal arms (front left and rear right) show tensile and bending stresses at their ends, induced by impact

inertia, while the rear left arm remains unloaded, indicating that the frame has not yet fully absorbed the impact energy. It is therefore recommended to extend the simulation to later times.

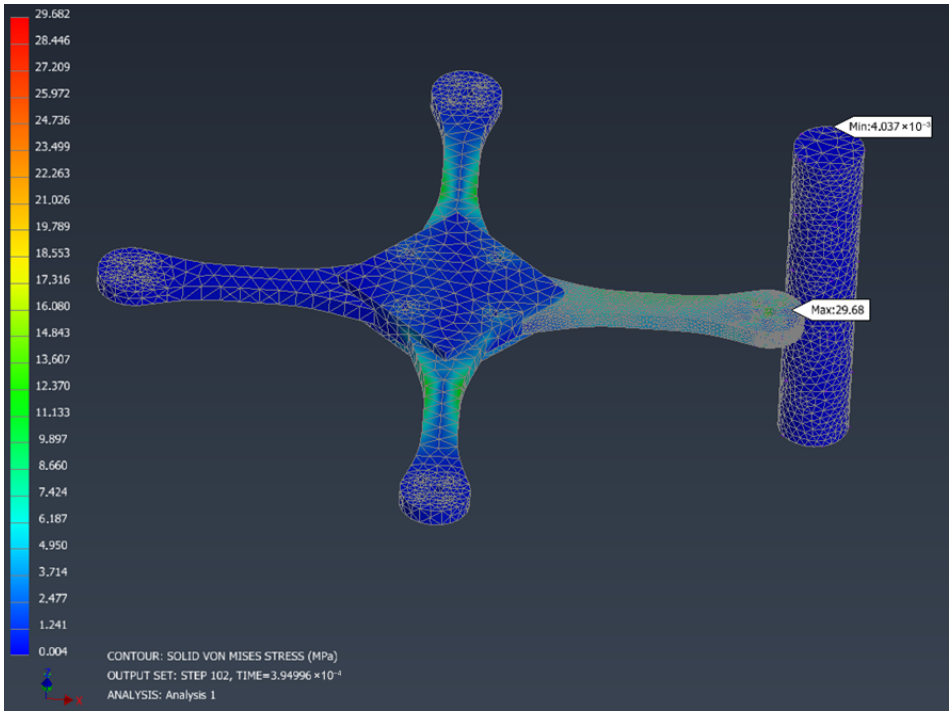

Figure 19. Von Mises stress representation of the frame at $t = 0.01$ s.

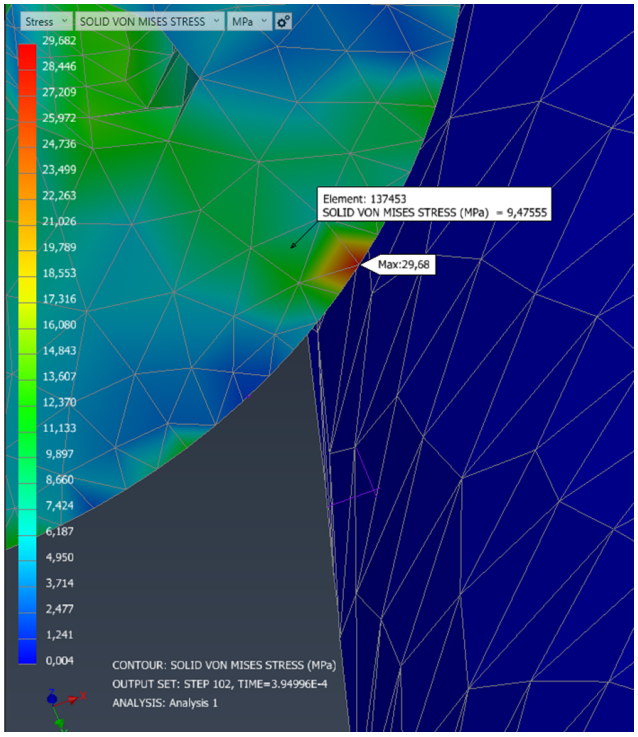

Figure 20. Detail of Von Mises stresses of the frame at $t = 0.01$ s.

The maximum recorded displacement is 2.393 mm (see Figure 21), concentrated in the cross arms, which move forward generating the stresses mentioned above.

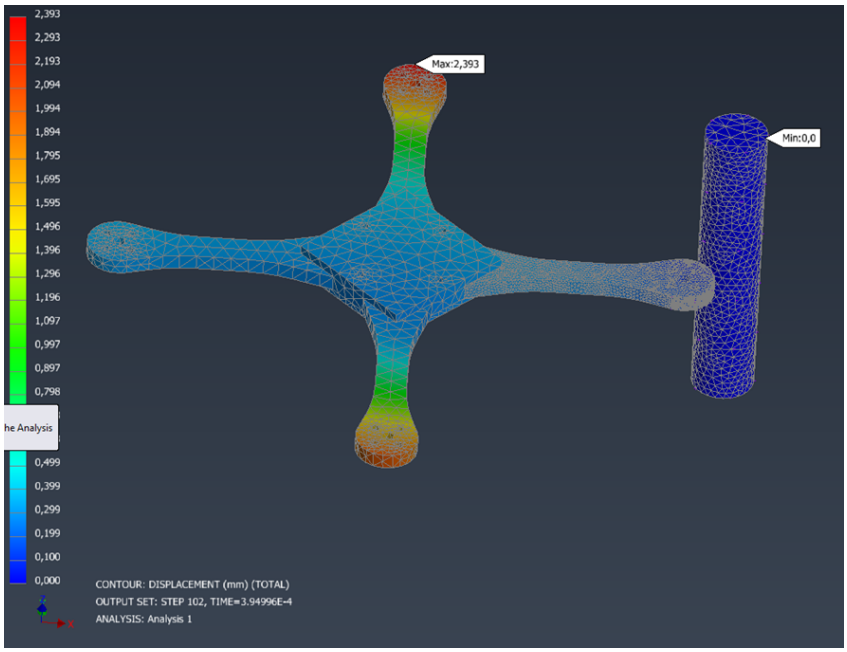

Figure 21. Frame displacement representation at $t = 0.01$ s.

- **Test at t = 1 s:**

To validate the hypothesis regarding the progressive absorption of impact energy, an additional simulation was carried out at $t = 1$ s, keeping the rest of the parameters unchanged. At this stage, it is observed that the rear-left arm presents a maximum displacement of 3.657 mm in the upward direction (see Figure 22), indicating that the drone has pitched forward as a consequence of the initial impact. This rotation is consistent with the expected dynamic behavior after a frontal collision.

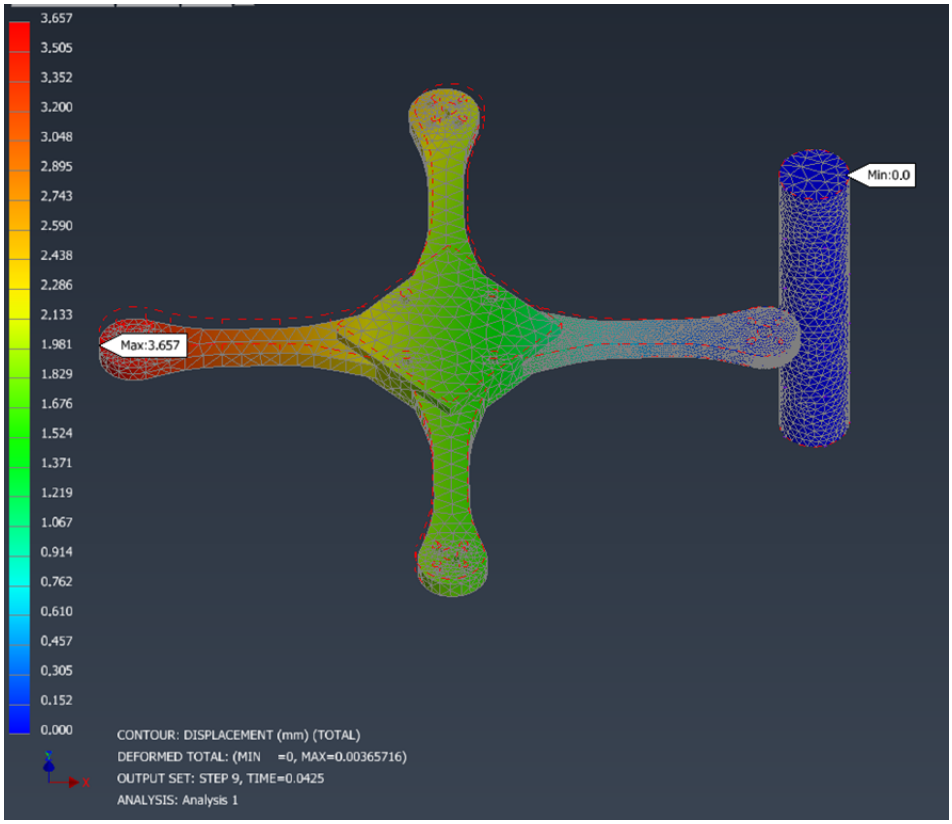

Figure 22. Frame displacement representation at $t = 1$ s.

The Von Mises stress reaches a maximum value of 41.78 MPa, located at the same point previously identified as a mesh stress concentration zone (see Figures 23 and 24). This increase confirms that this node continues to absorb most of the residual impact energy. On the other hand, the three arms not directly involved in the crash are completely unloaded, showing that the energy has been almost entirely absorbed by the impacted arm. This evolution confirms the initial hypothesis: the drone's structure channels the energy toward the front arm, enabling localized dissipation that protects the rest of the system.

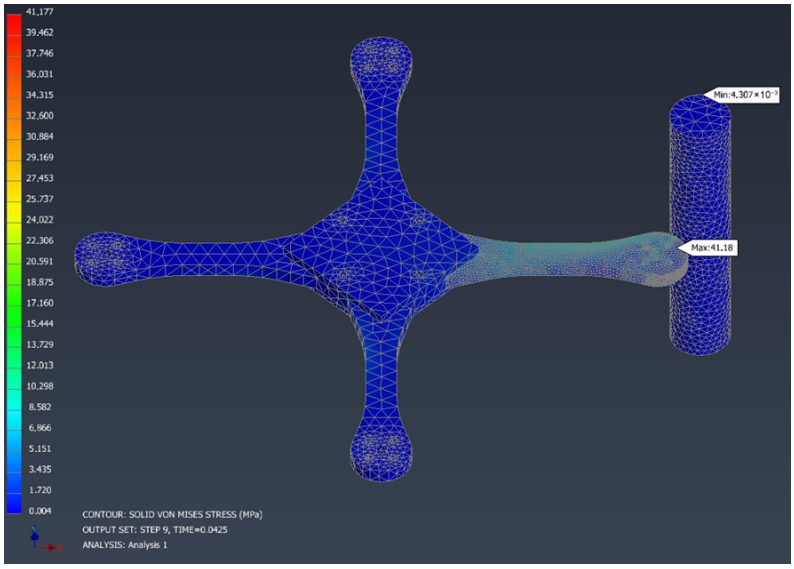

Figure 23. Von Mises stress representation of the frame at $t = 1$ s.

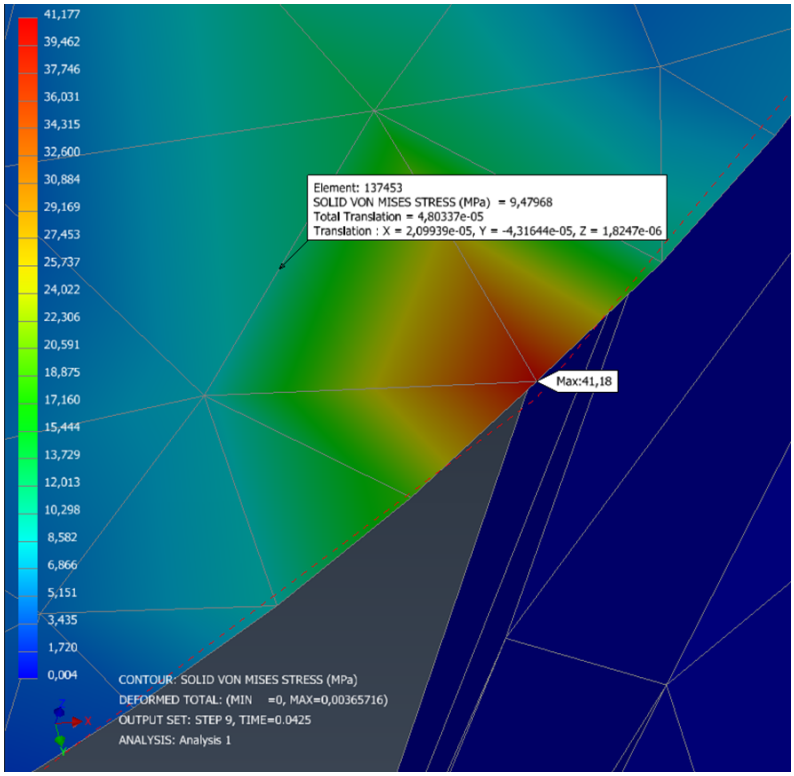

Figure 24. Detail of Von Mises stresses of the frame at $t = 1$ s.

It is worth noting that the node corresponding to element 137453, located in the impact zone, has been highlighted in order to analyze the origin of the maximum stress point observed in both simulations. This point coincides with the vertex of a region where the

mesh converges sharply, generating an artificial geometric discontinuity that acts as a stress concentrator. In both analyzed instants ($t = 0.01$ s, see Figure 20 and $t = 1$ s, see Figure 24), this element shows a Von Mises stress of 9.47 MPa, supporting the hypothesis that the high stress concentration recorded in that node is mainly due to the mesh configuration, and not to a real physical condition of the system. This analysis reinforces the need to refine the mesh in critical areas to avoid misinterpretations of structural behavior.

In Table 16, a comparative summary of the maximum displacements and stresses obtained in the two analyzed instants is presented, considering PETG as the base material with a yield strength of 40 MPa.

Table 16. Comparison of stresses and displacements at the analyzed instants (material: PETG).

Instant (s)	Maximum Displacement (mm)	Max. Von Mises (MPa)	Safety Factor (SF)
0.01	2.393	29.68	1.35
1.00	3.657	41.78	0.96

At $t = 0.01$ s, the Von Mises stress reaches 29.68 MPa, resulting in a safety factor of 1.35, which is acceptable though close to the limit. However, at $t = 1.00$ s, the maximum stress rises to 41.78 MPa, implying a safety factor of 0.96, i.e., slightly exceeding the yield strength of the material. It should be noted that this stress, as previously analyzed, is again concentrated in element `137453`, a zone where the mesh forms a sharp vertex. This configuration induces an artificial stress concentration. Therefore, it is concluded that the frame, from a structural point of view, would be safe were it not for this meshing anomaly. A further local mesh refinement in this region is recommended to avoid exaggerated stress readings that do not reflect the real behavior of the material. The safety factors have been calculated based on the PETG yield strength ($\sigma_{\text{adm}} = 40$ MPa):

$$\text{SF}_{0.01s} = \frac{\sigma_{\text{adm}}}{\sigma_{\text{Von Mises}}} = \frac{40}{29.68} = 1.35 \tag{11}$$

$$\text{SF}_{1.00s} = \frac{\sigma_{\text{adm}}}{\sigma_{\text{Von Mises}}} = \frac{40}{41.78} = 0.96 \tag{12}$$

- **Simplified beam model validation**

To validate the FEM results, a simplified estimation of the impact force was performed using the linear momentum principle:

$$F = \frac{\Delta p}{\Delta t} = \frac{m(v_f - v_i)}{\Delta t} \tag{13}$$

where $m = 0.25$ kg, $v_i = 11$ m/s, $v_f = 0$ m/s, and $\Delta t = 0.1$ s. The resulting average force is:

$$F = \frac{0.250 \cdot (0 - 11)}{0.1} = -27.5 \text{ N} \tag{14}$$

$$F = 27.5 \text{ N} \tag{15}$$

This value was applied in a static beam model: a cantilever of length $L = 70$ mm, rectangular cross-section $b = 10$ mm, $h = 5$ mm, subject to a 45° inclined load of 27.5 N.

The equivalent bending moment is:

$$M_{\text{eq}} = 1.924 \text{ Nm}$$

which leads to a maximum stress:

$$\sigma_{\max} = 23.08 \text{ MPa}$$

and maximum deflection:

$$\delta_{\max} = 2.55 \text{ mm}$$

A comparison with FEM simulations is provided in Table 17. The theoretical beam model yields conservative results, with higher stresses and deflections than observed in the full drone assembly, highlighting the structural reinforcement provided by geometry and joints. The corresponding Von Mises stress and displacement distributions are shown in Figures 25 and 26, respectively.

Table 17. Comparison of stresses and displacements under inclined static load of 27.5 N.

Case	Von Mises Stress (MPa)	Max. Displacement (mm)
Simplified beam (theory)	23.08	2.55
Individual arm (FEM)	11.16	1.716

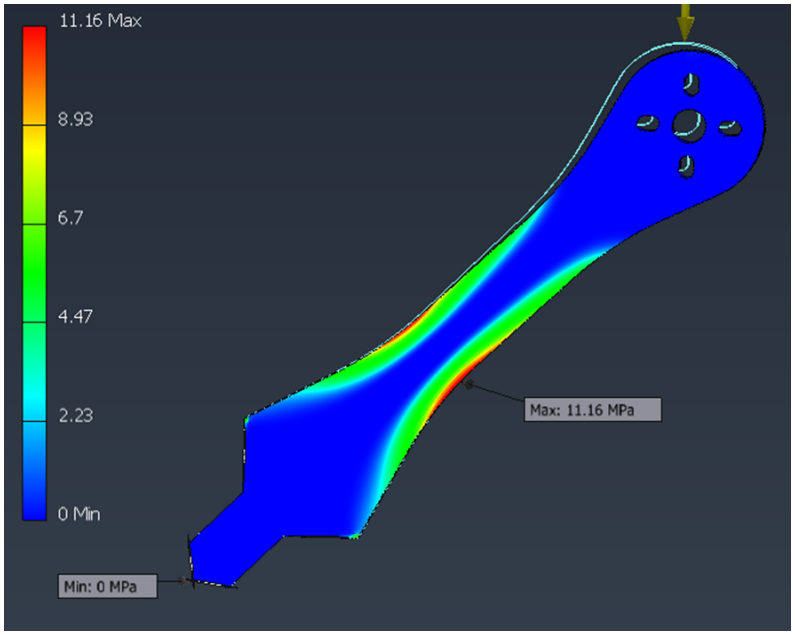

Figure 25. Von Mises stresses of the static analysis with $F = 27.5$ N at 45°.

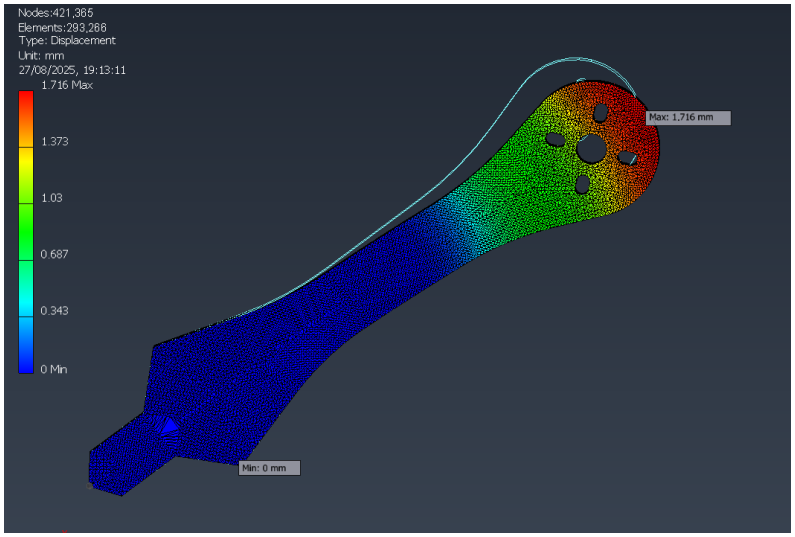

Figure 26. Displacements from static analysis with $F = 27.5$ N at 45°.

Experimental validation

To validate the numerical FEM model under a frontal impact condition equivalent to 40 km/h, a simplified experimental test was performed on a representative segment of the structural frame. The objective of this test was to confirm the order of magnitude of the deformation predicted by the simulations, rather than to obtain statistically representative data.

In the simplified FEM model, the dynamic impact was represented by a punctual load of 27.5 N, applied at an angle of 45° with respect to the horizontal axis. To replicate this in a static experimental setup, the applied load was decomposed into its components. The effective force acting along the principal direction of deformation is given by the following:

$$F_{\text{eff}} = 27.5\,\text{N} \cdot \cos(45^\circ) = 27.5 \times 0.7071 = 19.44\,\text{N}$$

This corresponds to the force exerted by a mass of approximately

$$m = \frac{F_{\text{eff}}}{g} = \frac{19.44}{9.81} = 1.98\,\text{kg}$$

Therefore, a physical load of 2 kg was used in the test, as shown in Figure 27.

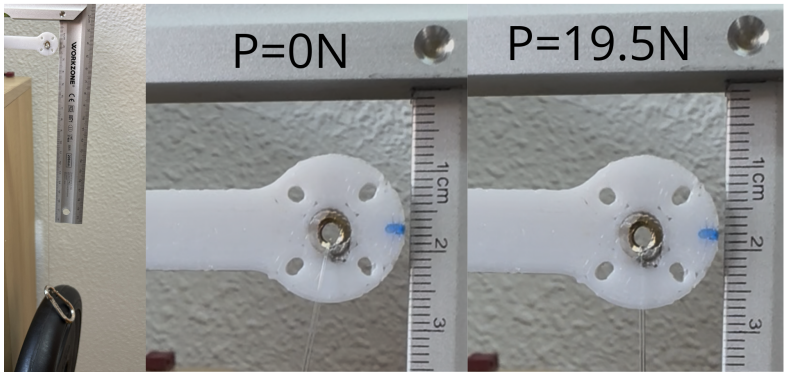

Figure 27. Static test setup reproducing the equivalent load of a 40 km/h frontal impact (2 kg ≈ 19.4 N).

The test configuration reproduced the same boundary conditions used in the FEM analysis: one end of the structure was rigidly clamped, and the load was applied at the opposite free end. The displacement was measured manually using a precision caliper, yielding a vertical deflection of approximately **1.25 mm**.

In comparison, the FEM simulation under identical loading conditions predicted a maximum displacement of **1.716 mm**. The deviation between experimental and numerical results can be attributed to the conservative assumptions made in the numerical model, where the material yield strength was intentionally underestimated to account for potential manufacturing imperfections and local stress concentrations. The comparison between the experimental and numerical results is summarized in Table 18.

Table 18. Comparison between experimental and FEM displacements under equivalent frontal impact load (19.44 N ≈ 2 kg).

Sample	Applied Load (N)	Measured Disp. (mm)	FEM Disp. (mm)	Error (%)
1	19.44	1.25	1.716	27.1

Although this test does not reproduce the transient nature of a real crash, it provides a reliable validation of the FEM predictions in terms of **stiffness and deformation magnitude**. The close agreement between experimental and numerical data supports the adequacy

of the simplified modeling approach and confirms that the structure remains within the elastic regime for loads representative of a 40 km/h frontal impact scenario.

In conclusion, this preliminary static test demonstrates the robustness of the FEM model and its capacity to predict realistic deformation levels under equivalent impact conditions, while emphasizing the need for future dynamic testing to capture transient stress distributions and damping effects.

Conclusions

As a conclusive result, the analysis identified the `maximum tension point (node)` as the most critical location for evaluating the structural integrity of the drone frame. This node is located on the inner face of the arm subjected to bending stress during the frontal impact, where the highest Von Mises stress value of **21.78 MPa** was recorded (see Figure 24).

Considering the PETG material's yield strength of approximately 40 MPa, the **safety factor** is calculated as:

$$SF = \frac{\sigma_y}{\sigma_{VM}} = \frac{40}{21.78} \approx 1.84$$

This value confirms that the frame remains within the elastic regime under the simulated conditions, providing a sufficient safety margin to prevent structural failure.

A summary of the most critical stress condition is presented in Table 19. The comparison between the nonlinear transient FEM model and the simplified static FEM model reveals significant differences in the predicted stress distribution and deformation response. The simplified model applies a **static point load**, which does not account for the **inertial effects** generated by the drone's mass during the impact event. Consequently, it overlooks the dynamic load transfer and energy absorption mechanisms that occur under real collision conditions. These discrepancies underline the necessity of performing a **nonlinear transient analysis**, capable of capturing the combined influence of inertia, time-dependent loading, and geometric nonlinearity, thus providing a more accurate and physically consistent representation of the structural behavior during impact.

Table 19. Summary of maximum stress and safety factor for the most critical node.

Critical Point	Von Mises Stress [MPa]	Safety Factor (SF)
Maximum tension point (inner arm face)	21.78	1.84

3.4.4. Nonlinear Transient Analysis: Free Take-Off of the Drone

This section presents the setup and results of the Finite Element Method (FEM) simulation, detailing the modeling approach, applied loads, and boundary conditions used to evaluate the drone's structural response during take-off.

- **FEM Study**

In this dynamic analysis, the structural behavior of the drone frame is studied under realistic take-off conditions. Unlike the previous maximum-thrust simulation case, the base of the model is unconstrained, allowing the system to accelerate vertically as a natural response to motor thrust.

Forces of 6.38 N per motor are applied (see Table 20), corresponding to the maximum thrust according to the data sheet. The total mass of the drone is 0.250 kg, and is coherently distributed in the model by the density adjustments described below.

The analysis is performed in Inventor Nastran using a nonlinear transient scheme, capturing accelerations, deformations, and both material and geometric nonlinear effects.

Table 20. Simulation conditions of the nonlinear transient analysis.

Parameter	Value
Thrust per motor	6.38 N
Total applied force	25.52 N
Drone mass	250 g
Analysis type	Nonlinear transient
Analysis duration	0.15 s
Constraints	Free body
Failure criterion	Von Mises

The analysis was configured using the numerical parameters listed in Table 21, where the applied mass adjustments are also presented.

Table 21. Numerical parameters used in the simulation.

Parameter	Value
Time step size	0.001 s
Number of steps	150
Rayleigh damping α	0.001
Rayleigh damping β	0.001

Mass distribution: although only part of the drone (core and arms) was simulated, densities were adjusted so that the model faithfully represents the total 250 g mass:

- Mass of arms and original cover: 38 g
- PETG density: 1.27 g/cm^3
- To balance the total mass, the density of the core cover was artificially increased to 22.352 g/cm^3, achieving a total mass of 250 g without using non-physical external gravity loads.
- **Results**

The peak values obtained during the analysis are summarized in Table 22. Maximum acceleration, velocity, and displacement are lower than predicted by theoretical models because part of the energy is absorbed by elastic deformations in the arms during ascent.

Table 22. Final results of the nonlinear transient analysis.

Quantity	Result	Unit
Final velocity	13.396	m/s
Maximum acceleration	89.285	m/s^2
Total displacement	1.007	m

The maximum Von Mises stress obtained was 7.576 MPa. Considering the PETG yield strength of 40 MPa, the safety factor is calculated as follows (see Table 23):

$$\mathrm{SF}_{\mathrm{dynamic}} = \frac{40\ \mathrm{MPa}}{7.576\ \mathrm{MPa}} = 5.28 \tag{16}$$

Table 23. Safety factor with respect to Von Mises stress.

Quantity	Result	Unit
Maximum Von Mises stress	7.576	MPa
PETG yield strength	40	MPa
Safety factor	5.28	–

In Figure 28, the Von Mises stresses, the first and third principal stresses, as well as the maximum deformation in the drone arms during free take-off, can be observed.

Table 24 compares the main mechanical results of a static fixed-base model versus the dynamic free-takeoff model.

Table 24. Comparison between static and dynamic analysis results.

Quantity	Static (fixed)	Dynamic (Take-Off)	Relative Difference
Max. Von Mises stress	7.25 MPa	7.576 MPa	+4.49%
First Principal stress (max.)	8.34 MPa	10.346 MPa	+24.03%
Third Principal stress (max.)	1.19 MPa	2.722 MPa	+128.66%
Max. total deformation	2.43 mm	0.45 mm	-81.48%
Safety factor	5.52	5.28	–4.35%

The comparison between the static and nonlinear transient analyses reveals that, although the *Von Mises* equivalent stress remains nearly unchanged in magnitude, the internal stress distribution experiences a marked transformation. In the transient case, the third principal stress (σ_3)—associated with local compression—increases significantly (from approximately -7.9 MPa in the static analysis to about -10.3 MPa), while the total displacement is substantially reduced due to the free-base condition during take-off. Consequently, the safety factor decreases slightly, from 5.52 to 5.28, reflecting a more realistic and demanding load scenario.

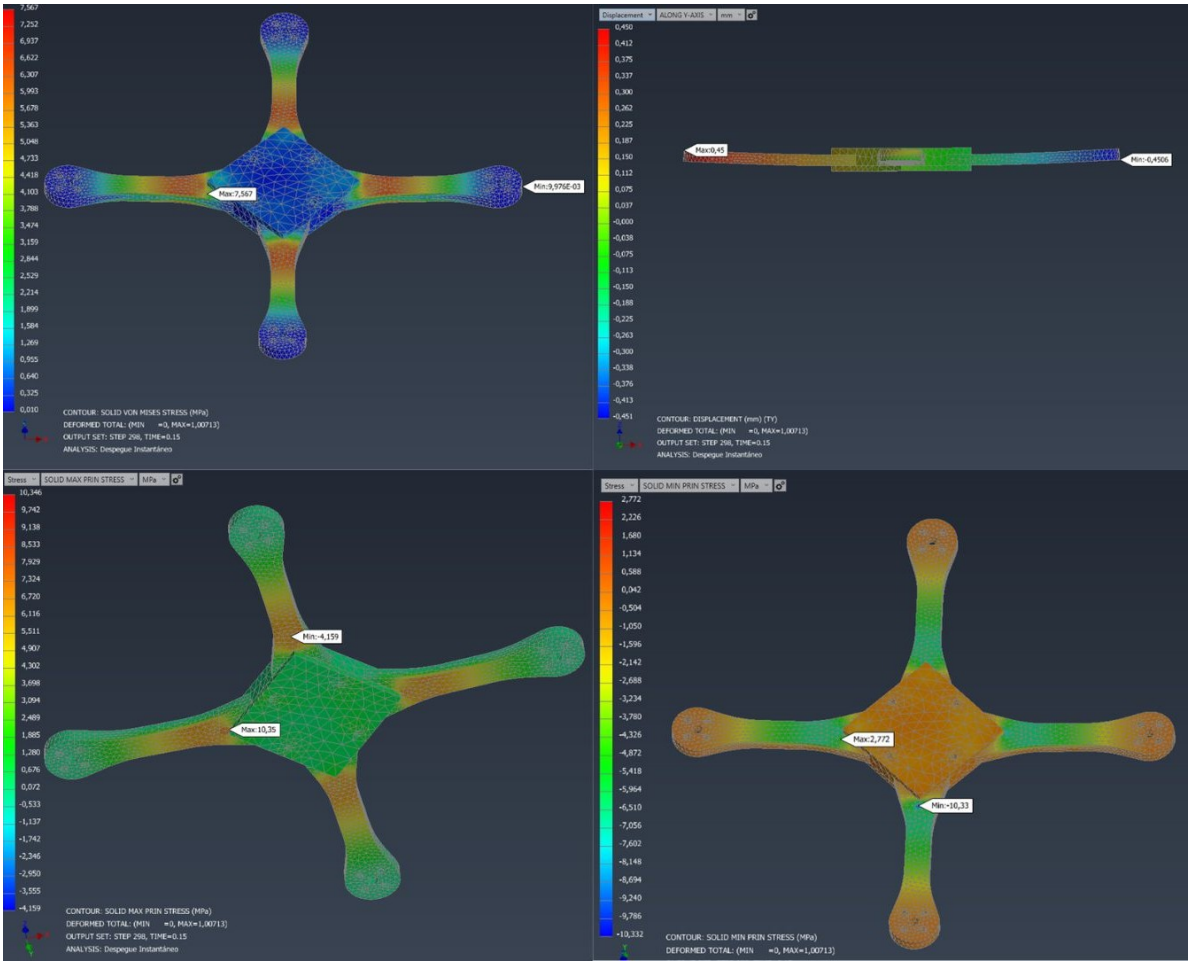

Figure 28. Stress, deformation distribution, and deformation during free take-off.

This behavior can be explained by the dynamic response of the structure when it is allowed to move freely. Under transient conditions, part of the external load is converted into acceleration rather than deformation, so the system exhibits lower global strain but

higher localized stresses. The inertial resistance of the mass acts to oppose deformation, concentrating compressive and shear stresses in specific regions such as the central hub and arm roots. Additionally, geometric reorientation and mode coupling between bending and torsion during motion generate complex triaxial stress states that amplify σ_3.

The fact that the *Von Mises* stress remains almost constant indicates that the total strain energy stored in the structure is similar between both analyses. However, its directional composition changes substantially: dynamic effects redistribute the load in space and time, producing higher compressive peaks without a proportional increase in the overall energy density. This explains why the transient case shows stronger local compression but comparable global stress magnitude.

In summary, the nonlinear transient analysis captures the realistic dynamic load redistribution that occurs during take-off: inertia reduces deformation but enhances local compression, modifying the internal stress balance and slightly reducing the global safety factor. This highlights the importance of performing transient dynamic simulations to accurately predict stress concentrations and potential critical regions in lightweight aerospace structures.

- **Simplified beam model validation**

This subsection validates the nonlinear transient analysis results by comparison with an analytical rigid-body model without damping, assuming instantaneous thrust application at $t = 0$.

Total thrust from four motors:

$$F_{\text{total}} = 4 \cdot 6.38 = 25.52 \text{ N}$$

Drone weight:

$$P = mg = 0.25 \cdot 9.81 = 2.4525 \text{ N}$$

Net upward force:

$$F_{\text{net}} = F_{\text{total}} - P = 25.52 - 2.4525 = 23.0675 \text{ N}$$

Resulting constant acceleration:

$$a = \frac{F_{\text{net}}}{m} = \frac{23.0675}{0.25} = 92.27 \text{ m/s}^2$$

Velocity after 0.15 s:

$$v(0.15) = a \cdot t = 92.27 \cdot 0.15 = 13.84 \text{ m/s}$$

Vertical displacement:

$$\delta(0.15) = \frac{1}{2}at^2 = \frac{1}{2} \cdot 92.27 \cdot (0.15)^2 = 1.038 \text{ m}$$

Simulation results (t = 0.15 s) using nonlinear transient analysis:

$$a_{\text{sim}} = 89.285 \text{ m/s}^2 \quad (17)$$

$$v_{\text{sim}} = 13.396 \text{ m/s} \quad (18)$$

$$\delta_{\text{sim}} = 1.00713 \text{ m} \quad (19)$$

A comparison between the analytical rigid-body calculations and the nonlinear transient simulation results is presented in Table 25, highlighting the differences in acceleration, velocity, and displacement of the drone during take-off.

Table 25. Comparison between analytical rigid-body model and nonlinear transient simulation.

Quantity	Analytical	Simulation	Relative Difference
Acceleration [m/s^2]	92.27	89.285	−3.23%
Velocity [m/s]	13.84	13.396	−3.17%
Displacement [m]	1.038	1.007	−2.97%

The comparison shows very good agreement between the nonlinear transient FEM simulation and the simplified analytical model. Slight differences are observed due to:

- Elastic deformation of the arms absorbing part of the thrust energy.
- Dynamic redistribution of mass in the flexible structure.
- Time integration and damping effects in the FEM solver.

Overall, the FEM model provides realistic results with a safety factor above 5, confirming the structural adequacy of the drone frame for take-off conditions.

3.4.5. Forward Flight Simulation: Pitch–Moment Maneuver

- **FEM Study**

To analyze the dynamic behavior of the drone during a forward manoeuvre, a nonlinear transient simulation was carried out in which a differential thrust is applied between the front and rear motors. This condition generates a *pitch* moment that tilts the drone forward, replicating the real operational mode during horizontal flight.

For this analysis, different forces are applied to the front and rear motors:

- Front motors (front left and right): 3.00 N.
- Rear motors (rear left and right): 4.00 N.

Given that the maximum thrust per motor is 6.38 N, the relative *throttle* percentage applied to each pair of motors is as follows:

$$\text{Throttle}_{\text{front}} = \frac{3.00}{6.38} \cdot 100 \approx 47.0\,\% \tag{20}$$

$$\text{Throttle}_{\text{rear}} = \frac{4.00}{6.38} \cdot 100 \approx 62.7\,\% \tag{21}$$

This thrust difference generates a net moment around the lateral axis (pitch), causing a forward tilt. In a real drone, this type of differential control is used precisely to induce forward movement while maintaining dynamic equilibrium.

During the simulation, the frame is fully released (no rigid constraints), allowing the free evolution of the system over time under these unbalanced forces. A nonlinear transient analysis is again employed to capture the interaction between inertia, acceleration, and structural deformation.

This scenario evaluates both the structural behavior of the frame under asymmetric dynamic conditions and the design feasibility during real control manoeuvres. The observed tilt in the simulation confirms that the model responds correctly to the applied moment, reproducing an initial forward trajectory as expected in real operation.

The simulation was performed with the same parameters as the maximum thrust study, using a time step of 0.001 s up to a total time of 0.15 s. The results at that instant are as follows:

- Maximum Von Mises stress: 4.438 MPa.
- Estimated safety factor: $\frac{22.0}{4.438} \approx 4.96$.
- Final velocity: 6.731 m s^{-1}.

- Approximate average acceleration: 44.67 m s^{-2}.
- Z-axis displacement: 0.514 m.
- X–Y plane displacement: 0.5 mm.

These results match the expected behavior: the differential thrust causes a slight tilt of the drone, but the applied *throttle* percentage is not sufficient to generate significant forward motion. Most of the displacement occurs along the vertical axis (Z), while horizontal translation (X–Y) is minimal. It is concluded that, at this thrust level, the induced *pitch* does not produce significant forward movement, indicating that a higher thrust difference or longer impulse duration would be necessary to achieve effective forward motion.

The simulation conditions for the pitch maneuver are summarized in Table 26, and a representative image of the FEM simulation is shown in Figure 29.

- **Results**

Table 26. Simulation conditions for forward maneuver with pitch moment.

Parameter	Value
Front thrust (per motor)	3.00 N
Rear thrust (per motor)	4.00 N
Front throttle (%)	47.0 %
Rear throttle (%)	62.7 %
Load direction	Vertical (unbalanced)
Expected result	Forward tilt (positive pitch)
Constraints	None (free body)
Analysis type	Nonlinear transient
Simulation duration	0.15 s
Integration step	0.001 s

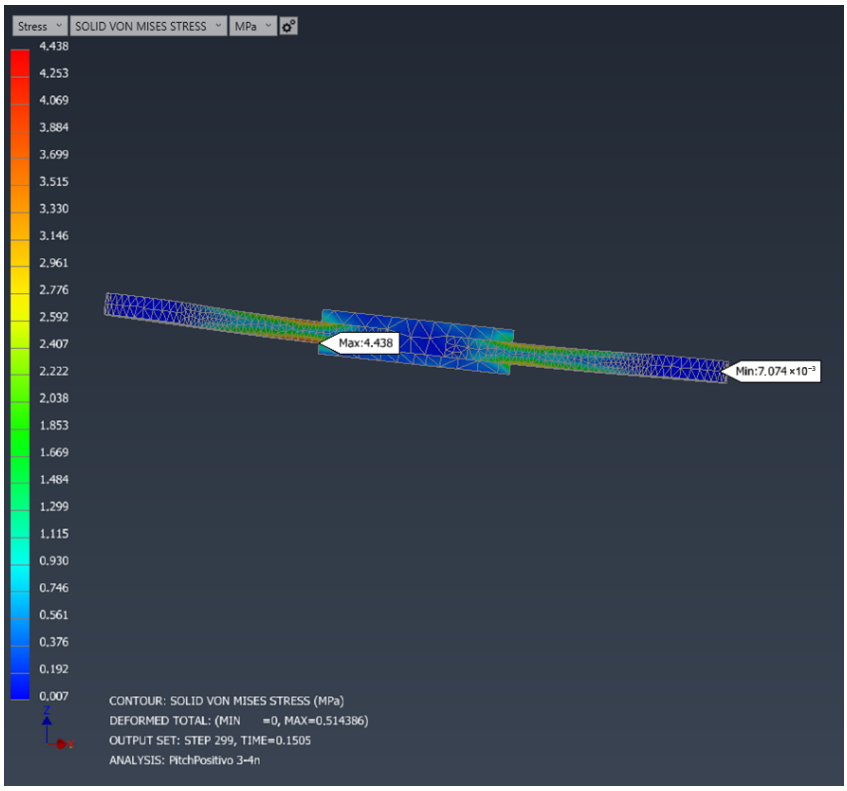

Figure 29. Von Mises stress distribution during forward manoeuvre.

- **Simplified beam model validation**

This section extends the model validation to a more complex control manoeuvre: a forward pitch ascent. Asymmetric thrust forces are applied instantaneously to the front and rear motors, generating both vertical acceleration and angular rotation. The objective is to compare the results with a rigid-body, undamped analytical model, evaluating both translational and rotational behavior of the drone, and to validate the fidelity of the non-linear transient FEM simulation. The corresponding displacement field obtained from the simulation is shown in Figure 30.

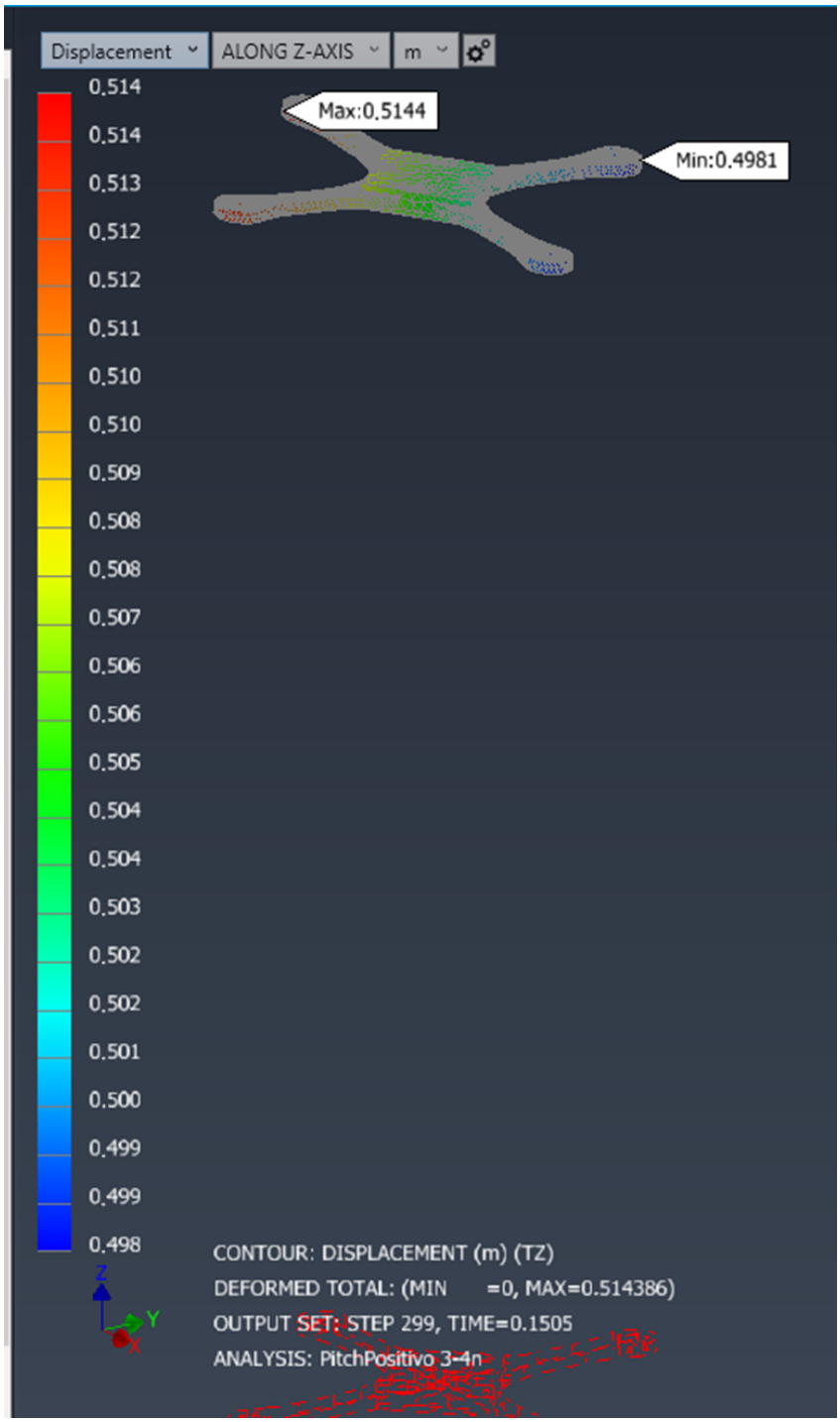

Figure 30. Total displacement map during forward manoeuvre.

At $t = 0$, the rear motors apply 4 N each, while the front motors apply 3 N each, generating a total thrust and a net pitching moment:

$$F_{\text{total}} = 2 \cdot 4 + 2 \cdot 3 = 14\,\text{N} \tag{22}$$

The drone weight is as follows:

$$P = mg = 0.25 \cdot 9.81 = 2.4525\,\text{N} \tag{23}$$

The net vertical force is therefore

$$F_{\text{net}} = F_{\text{total}} - P = 14 - 2.4525 = 11.5475\,\text{N} \tag{24}$$

Producing an ideal vertical acceleration of

$$a_z = \frac{F_{\text{net}}}{m} = \frac{11.5475}{0.25} = 46.19\,\text{m}\,\text{s}^{-2} \tag{25}$$

After 0.15 s, the corresponding velocity and displacement are as follows:

$$v_z(0.15) = a_z \cdot t = 46.19 \cdot 0.15 = 6.93\,\text{m}\,\text{s}^{-1} \tag{26}$$

$$\delta_z(0.15) = \frac{1}{2} a_z t^2 = \frac{1}{2} \cdot 46.19 \cdot (0.15)^2 = 0.519\,\text{m} \tag{27}$$

The asymmetric thrust produces a torque about the pitch axis. Considering the front–rear distance $L = 0.127$ m, the resulting moment is as follows:

$$\tau_{\text{pitch}} = (F_{\text{rear}} - F_{\text{front}}) \cdot \frac{L}{2} = (8 - 6) \cdot 0.0635 = 0.127\,\text{N}\,\text{m} \tag{28}$$

With a moment of inertia $I = 0.003\,\text{kg}\,\text{m}^2$, the angular acceleration is as follows:

$$\alpha = \frac{\tau}{I} = \frac{0.127}{0.003} = 42.33\,\text{rad}\,\text{s}^{-2} \tag{29}$$

Integrating over the time interval $t = 0.15$ s gives the following:

$$\omega(0.15) = \alpha \cdot t = 42.33 \cdot 0.15 = 6.35\,\text{rad}\,\text{s}^{-1} \tag{30}$$

$$\theta(0.15) = \frac{1}{2} \alpha t^2 = \frac{1}{2} \cdot 42.33 \cdot (0.15)^2 = 0.475\,\text{rad} = 27.2^\circ \tag{31}$$

Hence, the inclination angle after 0.15 s is approximately 27.2°. Using this value, the horizontal acceleration becomes as follows:

$$a_x = a_z \cdot \sin(\theta) = 46.19 \cdot \sin(27.2^\circ) = 21.1\,\text{m}\,\text{s}^{-2} \tag{32}$$

and the corresponding horizontal displacement at $t = 0.15$ s is as follows:

$$\delta_x(0.15) = \frac{1}{2} a_x t^2 = \frac{1}{2} \cdot 21.1 \cdot (0.15)^2 = 0.237\,\text{m} \tag{33}$$

The simulation was carried out in Inventor Nastran under the same conditions as those used in the previous section, but the thrusts were modified according to the asymmetric configuration (4 N rear, 3 N front). The results at $t = 0.15$ s were as follows:

$$a_{z,\text{sim}} = 44.67\,\text{m}\,\text{s}^{-2} \tag{34}$$

$$v_{z,\text{sim}} = 6.73\,\text{m}\,\text{s}^{-1} \tag{35}$$

$$\delta_{z,\text{sim}} = 0.514\,\text{m} \tag{36}$$

$$\delta_{x,\text{sim}} = 0.214\,\text{m} \tag{37}$$

The comparison between the analytical and FEM simulation results is shown in Table 27.

Table 27. Comparison between analytical model and FEM simulation for the pitch manoeuvre.

Quantity	Analytical	Simulation	Difference (%)
Vertical acceleration (m/s^2)	46.19	44.67	3.3
Vertical velocity (m/s)	6.93	6.73	2.9
Vertical displacement (m)	0.519	0.514	1.0
Horizontal displacement (m)	0.237	0.214	9.7
Pitch angle (°)	27.2	25.8	5.2

The differences between analytical and FEM results remain below 10%, confirming the physical consistency of the model. The small deviations are mainly attributed to the structural flexibility of the drone arms, which absorb part of the mechanical energy during thrust application. This causes slightly lower accelerations and displacements compared to the ideal rigid-body prediction, a behavior consistent with real physical response.

The results demonstrate that the structural model behaves coherently under asymmetric thrust, reproducing both the expected vertical motion and the onset of pitch rotation. The good agreement between analytical and numerical results confirms the model's validity for simulating dynamic manoeuvres, supporting its application to more complex control and flight analyses.

3.5. Flight Tests

To complement the numerical and simulation analyses presented in previous sections, experimental flight tests were conducted with the PETG prototype. These tests aimed to verify the dynamic behavior, stability, and performance of the system under both GPS-assisted and manual aggressive flight conditions.

The flight data were obtained through onboard logs recorded by the Flight Controller and post-processed to extract representative velocity and acceleration profiles. Figure 31 shows the GPS-based velocity traces recorded during a typical test flight, while Figure 32 illustrates the measured peak accelerations achieved during high-thrust maneuvers

The prototype flies correctly and the chassis withstands the loads experienced during flight, including accelerations up to 4.2 g ($41.19\,m\,s^{-2}$), abrupt changes in direction, and high-speed maneuvers reaching approximately $116\,km\,h^{-1}$.

These flight results further substantiate the proposed model and provide practical evidence of the prototype's reliability and robustness under realistic conditions. The images presented correspond to captures from the analog On-Screen Display (OSD) of the onboard Video Transmitter (VTX), directly recorded during the test flights. An extra video is available in the Supplementary Materials.

Figure 31. GPS-based max velocity of 116 km/h recorded during flight tests.

Figure 32. Measured peak acceleration of 4.2G during aggressive flight maneuvers.

4. Study Limitations

Despite the comprehensive methodology and validation workflow implemented in this study, several limitations should be acknowledged. First, the finite element analyses were based on an isotropic approximation of PETG mechanical properties, while FDM-printed polymers exhibit marked anisotropy depending on print orientation and process parameters. Although this assumption provided a conservative lower-bound estimate of stiffness and strength, it does not fully capture interlayer delamination or shear failure modes, which could influence real-world crash performance.

Second, while experimental validation was conducted through static bench tests and flight trials, the number of samples was limited and did not include statistical variability or long-term fatigue evaluation. Fatigue, thermal aging, and repeated impact behavior remain unexplored and could significantly affect the service life of the chassis, especially in PETG prototypes.

Third, impact simulations were performed under idealized boundary conditions, assuming a rigid obstacle and neglecting aerodynamic damping and energy dissipation through attached components such as motors and propellers. This simplification might

overestimate stress magnitudes at localized regions. Furthermore, the nonlinear transient FEM used mesh discretization that introduced artificial stress concentrations, as identified in the analysis of the impact node, potentially skewing maximum stress values.

Another limitation lies in the scope of materials considered. The study focused on PETG for prototyping and quasi-isotropic carbon fiber composites for production, but did not explore intermediate or hybrid materials such as carbon-fiber-reinforced polymers with adjustable layups, which could optimize the trade-off between manufacturability and performance.

Lastly, aerodynamic effects, vibration coupling with electronic components, and control feedback dynamics were not included in the structural model. These factors could alter resonance frequencies and load distributions during real flight, requiring future integration of multi-physics co-simulation frameworks (structural–aerodynamic–control).

Addressing these limitations through extended experimental campaigns, fatigue and vibration testing, anisotropic material modeling, and coupled multi-physics simulations would enhance the robustness and predictive accuracy of future designs.

5. Conclusions

This work presented the complete design, fabrication, and structural validation of a sub-250 g FPV drone chassis through an integrated workflow combining CAD modeling, additive manufacturing, and advanced finite element simulations. The chassis was developed using FDM 3D printing in PETG, enabling low-cost and iterative prototyping, while nonlinear static and transient FEM analyses—including impact simulations at 5 m/s—provided a realistic assessment of its structural performance.

Experimental validation through static and flight tests confirmed that the proposed frame withstands operational stresses with safety factors above acceptable limits, demonstrating functional robustness during high-speed manoeuvres and impact conditions. The comparison with carbon fiber composite simulations further established the feasibility of transitioning toward lightweight, high-stiffness production models, achieving over 98% reduction in deformation and a seven-fold increase in safety margins relative to PETG.

The proposed design philosophy—screwless, modular, and inspired by traditional joinery—proved effective for maintenance, interchangeability, and structural resilience. Moreover, the workflow integrates firmware-linked validation, bridging the gap between numerical prediction and real-flight performance.

In conclusion, this study delivers a validated and scalable methodology for developing lightweight UAV structures that unite simulation-driven design, experimental verification, and practical manufacturability, setting a foundation for subsequent research in advanced materials, anisotropic modeling, and coupled aero-structural–control simulations.

Supplementary Materials: The following supporting information can be downloaded at: https://www.mdpi.com/article/10.3390/drones9110789/s1, Video S1: Return-to-Home Autonomous Flight Test., Video S2: Peak Acceleration, Velocity, and Hard Maneuver Tests.

Author Contributions: Conceptualization, B.M.A.-H. and S.A.F.; methodology, B.M.A.-H. and S.A.F.; software, S.A.F.; validation, B.M.A.-H.; formal analysis, B.M.A.-H. and S.A.F.; investigation, B.M.A.-H. and S.A.F.; resources, S.A.F.; data curation, S.A.F.; writing—original draft preparation, B.M.A.-H. and S.A.F.; writing—review and editing, B.M.A.-H. and S.A.F.; visualization, B.M.A.-H.; supervision, B.M.A.-H.; project administration, B.M.A.-H. and S.A.F. All authors have read and agreed to the published version of the manuscript.

Funding: This research received no external funding.

Data Availability Statement: The original contributions presented in this study are included in the article/Supplementary Materials. Further inquiries can be directed to the corresponding author.

Conflicts of Interest: The funders had no role in the design of the study; in the collection, analyses, or interpretation of data; in the writing of the manuscript; or in the decision to publish the results.

Abbreviations

The following abbreviations are used in this manuscript:

AIO	All-in-One
BEC	Battery Eliminator Circuit
BLDC	Brushless Direct Current
Brushless	Brushless Motor
CDG	Center of Gravity (Spanish: Centro de Gravedad)
COG	Center of Gravity
ELRS	Express Long-Range System
ESC	Electronic Speed Controller
FEA	Finite Element Analysis
FDM	Fused Deposition Modeling
PETG	Polyethylene Terephthalate Glycol-modified
CFRP	Carbon Fiber Reinforced Polymer
FC	Flight Controller
FEM	Finite Element Method
fem	Electromotive Force (Spanish: Fuerza Electromotriz)
FRAME	Drone Frame (drone structure)
FPV	First Person View
IMU	Inertial Measurement Unit
MCU	Microcontroller Unit
MOSFET	Metal–Oxide–Semiconductor Field-Effect Transistor
PID	Proportional Integral Derivative
PWM	Pulse Width Modulation
QUAD	Quadcopter (four-propeller drone)
UAV	Unmanned Aerial Vehicle
VTX	Video Transmitter
WiFi	Wireless Fidelity
CAD	Computer-Aided Design
CLI	Command Line Interface
OSD	On-Screen Display
VDC	Volt Direct Current
Tx	Transmitter
Rx	Receiver
RSSI	Received Signal Strength Indicator
DVR	Digital Video Recorder
TMC	Thermal Motor Coefficient
STL	Stereolithography File Format
.ipt	CAD Part File (Autodesk Inventor)
.iam	CAD Assembly File (Autodesk Inventor)
.idw	2D Drawing File (Autodesk Inventor)

References

1. Kumar, V.; Singh, H.; Kumar, R. PETG/carbon fiber composites with different structures produced by 3D printing. *Polym. Test.* **2023**, *117*, 107003.
2. Floreano, D.; Wood, R.J. Science, technology and the future of small autonomous drones. *Science* **2015**, *349*, 1–6. [CrossRef] [PubMed]
3. Zhao, Y.; Chen, J.; Wang, X.; Yang, Q. Dynamic response and vibration analysis of lightweight UAV structures made of composites. *Compos. Struct.* **2019**, *220*, 802–812.

4. Ammar, A.; Benali, A.; Naceur, H. Mechanical performances of printed carbon fiber-reinforced PLA and PETG composites. *J. Compos. Mater.* **2024**, *238*, 1488–1499. [CrossRef]
5. Goyal, R.; Gupta, S.; Reddy, P.S. Digital twin-based structural health monitoring for unmanned aerial vehicles. *Aerosp. Sci. Technol.* **2021**, *118*, 107023.
6. Wahid, K.A.; Iqbal, M.W.; Khan, M.A. A review of lightweight materials for UAV airframes. *Mater. Today Proc.* **2021**, *47*, 3832–3838.
7. Wang, L.; Zhang, H.; Zhou, M. Simulation-driven design optimization of UAV structures manufactured by additive manufacturing. *Addit. Manuf.* **2020**, *34*, 101200.
8. Li, X.; Sun, Y.; Zhou, Y.; Huang, G. Mechanical performance of carbon fiber composites for lightweight UAV applications. *Mater. Des.* **2022**, *214*, 110400.
9. Pérez, J.; Martín, A.; Rodríguez, F. Lightweight structural optimization and validation of UAV composite frames. *J. Intell. Robot. Syst.* **2023**, *107*, 75.
10. MohamedZain, A.O.; Chua, H.; Yap, K.; Uthayasurian, P.; Jiehan, T. Novel Drone Design Using an Optimization Software with 3D Model, Simulation, and Fabrication in Drone Systems Research. *Drones* **2022**, *6*, 97. [CrossRef]
11. Singh, R.; Kumar, R.; Mishra, A.; Agarwal, A. Structural Analysis of Quadcopter Frame. *Mater. Today Proc.* **2020**, *22*, 3320–3329. [CrossRef]
12. Nvss, S.; Esakki, B.; Yang, L.-J.; Udayagiri, C.; Vepa, K.S. Design and Development of Unibody Quadcopter Structure Using Optimization and Additive Manufacturing Techniques. *Designs* **2022**, *6*, 8. [CrossRef]
13. Shelare, S.D.; Aglawe, K.R.; Khope, P.B. Computer Aided Modeling and Finite Element Analysis of 3-D Printed Drone. *Mater. Today Proc.* **2021**, *47*, 3375–3379. [CrossRef]
14. Al-Haddad, L.A.; Jaber, A.A.; Giernacki, W.; Khan, Z.H.; Ali, K.M.; Tawafik, M.A.; Humaidi, A.J. Quadcopter Unmanned Aerial Vehicle Structural Design Using an Integrated Approach of Topology Optimization and Additive Manufacturing. *Designs* **2024**, *8*, 58. [CrossRef]
15. Federal Aviation Administration (FAA). Remote Identification of Unmanned Aircraft; Final Rule. *Fed. Regist.* **2023**, *88*, 430–456.
16. European Union Aviation Safety Agency (EASA). Easy Access Rules for Unmanned Aircraft Systems (Regulations (EU) 2019/947 and 2019/945). *EASA Publ.* **2023**.
17. Azambuja, R.d.; Fouad, H.; Bouteiller, Y.; Sol, C.; Beltrame, G. When Being Soft Makes You Tough: A Collision-Resilient Quadcopter Inspired by Arthropods' Exoskeletons. *arXiv* **2021**, arXiv:2103.04423.
18. Lanzotti, A.; Martorelli, M.; Staiano, G. The Influence of FDM Process Parameters on Tensile Strength of PETG Parts. *Materials* **2021**, *14*, 2623. [CrossRef]
19. ASM International. *ASM Handbook, Volume 21: Composites*, 2nd ed.; ASM International: Materials Park, OH, USA, 2019.
20. Huang, J.; Zhang, D.; Liu, W. Mechanical Characterization of Quasi-Isotropic Carbon Fiber/Epoxy Laminates for UAV Frame Applications. *J. Compos. Mater.* **2020**, *54*, 2765–2778.
21. Akano, T.T.; Soremekun, G.A.; Shitta, M.B.; Oke, S.A. The Deformation Response of a Functional Four-Cylinder Reciprocating Engine using FEM and a Surrogate Model. *J. Eng. Sci. Technol. Rev.* **2023**, *16*, 59–65. [CrossRef]
22. Doğan, S.Ö.; Anık, B.G.; Göktaş, U. Vertical Water Silo Design and Analysis. *Int. J. Comput. Exp. Sci. Eng. (IJCESEN)* **2023**, *9*, 313–319.
23. Ghimouz, C.; Kenné, J.P.; Hof, L.A. On Sustainable Design and Manufacturing for the Footwear Industry—Towards Circular Manufacturing. *Mater. Des.* **2023**, *233*, 112224. [CrossRef]
24. Mereuta, V. Static Analysis of Wheel Rim Using Inventor Software. *Int. J. Res. Appl. Sci. Eng. Technol. (IJRASET)* **2021**, *9*, 516–521. [CrossRef]
25. Mereuta, V. Analysis of Torsen Differential Using Autodesk Inventor Nastran. *Int. J. Res. Appl. Sci. Eng. Technol. (IJRASET)* **2023**, *11*, 829–835. [CrossRef]
26. Sepahi, M.; Abusalma, H.; Jovanovic, V.; Eisazadeh, H. Mechanical Properties of 3-D-Printed Parts Made of Polyethylene Terephthalate Glycol. *J. Mater. Eng. Perform.* **2021**, *30*, 4813–4823. [CrossRef]
27. Özen, A.; Ganzosch, G.; Barchiesi, E.; Auhl, D.W.; Müller, W.H. Investigation of Deformation Behaviour of PETG-FDM-Printed Metamaterials. *SAGE Open Eng.* **2021**, *10*, 1–14.
28. Kumar, S.; Singh, R.; Ahuja, I.P.S. Effect of Printing Parameters on the Thermal and Mechanical Properties of 3D-Printed PLA and PETG Using Fused Deposition Modeling. *Polymers* **2021**, *13*, 1758. [CrossRef]
29. Özen, A.; Auhl, D.A. Modeling of the Mechanical Properties of Fused Deposition Modeling (FDM) Printed Fiber-Reinforced Thermoplastic Composites. *SAGE Open Eng.* **2022**, *12*, 1–13. [CrossRef]
30. Zhang, Y.; Chen, H.; Li, J.; Wang, P. Mechanical Properties and Numerical Simulation of FDM 3D-Printed PETG/Carbon Composite Unit Structures. *J. Mater. Res. Technol.* **2023**, *23*, 656–669.
31. Ahmed, H.; Zhao, Y.; Kumar, R. Evaluation of Mechanical Properties of 3D-Printed PETG and Polyamide (6) Polymers. *Chem. Phys. Impact* **2024**, *8*, 100491.

32. Seibel, S.; Kiendl, T. A finite element approach for modelling the fracture. In *Progress in Additive Manufacturing*; Springer: Berlin/Heidelberg, Germany, 2025.
33. Somireddy, M.; Czekanski, A.; Atre, S. Modelling of Failure Behaviour of 3D-Printed Composite Parts. *Appl. Sci.* **2022**, *12*, 10724. [CrossRef]
34. Gonabadi, H.; Zamani Miandashti, M.; Oila, A. Micro-mechanical characterisation of 3D-printed composites via nano-indentation and finite-element homogenization techniques. In *Progress in Additive Manufacturing*; Springer: Berlin/Heidelberg, Germany, 2025.
35. Chen, Y.; Ye, L. Path-Dependent Progressive Failure Analysis for 3D-Printed Continuous Carbon Fibre Reinforced Composites. *Chin. J. Mech. Eng.* **2024**, *37*, 72. [CrossRef]